Instituto Tecnológico y de Estudios Superiores de Monterrey

Campus Monterrey

School of Engineering and Sciences

Mechanistic study of methanol electro-oxidation on nickel thin films

A thesis presented by

María Paula Salinas Quezada

Submitted to the

School of Engineering and Sciences

in partial fulfillment of the requirements for the degree of

Master of Science

in

Nanotechnology

Monterrey, Nuevo León, June, 2020

ABSTRACT

Self-terminated nickel electrodeposition was studied on gold microelectrodes in the presence of sulfate and chloride ions. The voltammograms in both electrolytes conditions revealed a sharp current spike that was correlated with the self-termination of Ni electrodeposition and the onset of the H_2O reduction.

Thin-layers of nickel were electrodeposited onto polycrystalline gold electrodes using current pulses on electrolytes containing 50 mM $NiSO_4$. The behavior of the potential transients was the same as previously reported by our group. The potential transients curves during the nickel electrodeposition suggest that the nucleation process occurs in a time scale at which the surface area determines the diffusion field, while the geometric area is the one defining the diffusion field during the growth of the nuclei.

Gold electrodes modified with electrodeposited nickel films and nickel wire were activated by continuous cycling (30 cycles) in alkaline media. The formation of two anodic peaks around 0.35 and 0.407 V vs. Ag|AgCl were observed, suggesting the formation of different NiOOH structures α/γ or β/β. The higher catalytic activity for methanol oxidation ($EI = 136.2$ mA cm^{-2}) was obtained when the deposits that gave the higher β character. Therefore, we can infer that electrodes with higher proportions of β-NiOOH than γ-NiOOH are more active material for methanol oxidation.

Finally sampled current voltammetry technique was employed to complement the study of the activation of the nickel surface and its methanol oxidation mechanism, confirming that the highest activity for methanol oxidation was achieved when higher proportions of β-NiOOH were on the surface, however at these conditions the deposits also showed higher catalytic activity for oxygen evolution reaction.

ACKNOWLEDGEMENTS

of teamwork. Finally, thank María Gabriel, Juan Carlos, Jose (Chozita) and Rosita for always being there for me, for your friendship and empathy a long these years. I will never forget the experiences we have shared.

DEDICATION

This thesis work is dedicated to my beloved parents; thank you for giving me "roots to know where home is and wings to fly free". Mamita, thank you for encouraging me to pursue my dreams and never allow me to give up. Thank you for giving me invaluable educational opportunities, and inspire me to face the eventualities of life with determination, enthusiasm, and fear of God. Viejito, thank you for always believing in me, even when I do not believe in myself. My siblings, Claudya, Karen, and Pablo, thank you for always supporting me at a distance, for always celebrating my achievements and mourning my failures and for never leaving me alone. I also dedicate my thesis to Doménica and Pablo Andrés, whose I love them with my life, thank you for making me the proudest and happiest aunt in the world. Last but not the least, I dedicate my thesis to this special person, who has been patient with me when I'm frustrated. Thank you for celebrating with me when even the littlest things go right, and you are there whenever I need you to just listen.

Contents

List of Tables

List of Figures

Chapter 1

Introduction

Only 15.5% of Mexico's electricity [1] comes from renewable sources. Fossil fuels such as oil and coal remain the dominant natural source to cover the country's energy needs [2, 3]. The excessive use of these non-renewable fuels has increased production of CO_2, contributing directly to air pollution and greenhouse effects [4]. This has brought renewable energy to the forefront of the energy landscape.

Renewable energy, such as fuel cells, offers cleaner and more effective alternatives to combustion [5]. Fuel cells have many inherent advantages over traditional combustion-based systems such as the basic module-based system that allows for simple construction of a diverse range of portable or stationary power generation applications, making fuel cells one of the strongest candidates to be the energy conversion device of the future [6, 5].

Because of this, the global fuel cell market size has increased considerably in the past decade [1, 4]. Direct methanol fuel cells, particularly the reaction mechanism of methanol oxidation and the role of the electrocatalyst in this reaction are of the main interest of the present work.

1.1 Fuel cells

Fuel cells are electrochemical energy conversion devices; through an electrochemical reaction, these transform the chemical energy of a fuel and an oxidizing agent into electrical energy [7, 8]. While batteries are also electrochemical energy conversion devices, it is important to emphasize their differences with fuel cells. Batteries are used as energy storage and conversion devices with limited lifetimes [6]. On the other hand, fuel cells are used only for energy conversion, whereby they can keep running as long as the reactants are sufficiently supplied, and the products are correctly removed.

The essential elements of a fuel cell are two electrodes, known as anode and cathode, and an ion-conducting electrolyte, sandwiched between them. Together, these three parts are known as the membrane electrode assembly (MEA) [9]. A schematic representation of a methanol fuel cell is shown in Figure 1.1.
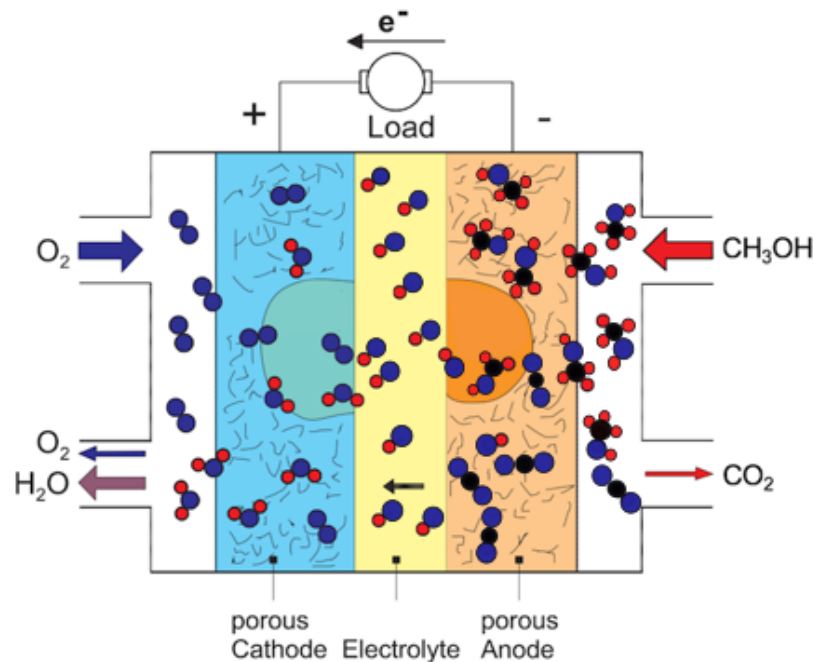
Figure 1.1: Scheme of a direct methanol fuel cell in alkaline medium. Adapted from [10].

In the simplest scenario (Figure 1.1), a fuel such as methanol is fed into the anode compartment and an oxidant, commonly a flow of air or oxygen, into the cathode

compartment [11]. The fuel is oxidized and the oxidizing agent is reduced. The electrolyte assists as a barrier to avoid gas diffusion; however, it allows the migration of ions across the membrane. The electrodes are made of a high surface area conductive material, such as carbon cloth, that serve as support for the electrocatalyst. The latter provides the active sites for the charge transfer reactions; thus, they determine, in large part, the efficiency of the fuel cell [12].

The first fuel cell was developed by William Grove, the father of the fuel cell science, who demonstrated that the electrochemical combination of hydrogen with oxygen produces electricity [12, 6]. Grove accidentally discovered the reverse process of electrolysis when he disconnected the battery from the electrolyzer, as shown in Figure 1.2a), and connected the two electrodes, causing a current flow in the opposite direction (Figure 1.2b) [13].
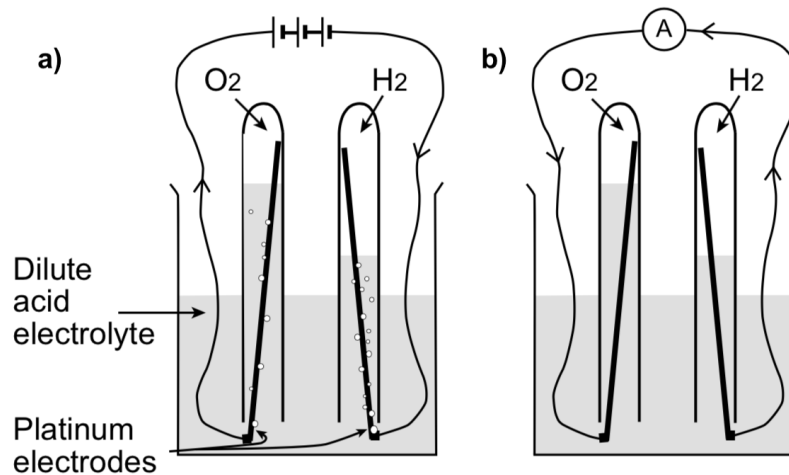
Figure 1.2: a) The principle of an electrolyzer and b) a fuel cell. Taken from [12].

Nonetheless, due to the corrosion and instability of the used materials, this type of fuel cells was not practical for commercial applications. In 1950, Thomas Bacon improved the fuel cell [14]; he replaced the sulfuric acid electrolyte for potassium hydroxide and constructed porous nickel electrodes to substitute the platinum electrodes of the previous design [13]. This allowed gas diffusion through the electrode and improved the contact area between the electrolyte, the electrode, and the gases, thus increasing the power density of the fuel cell.

Almost two centuries of scientific research have led to the development of fuel cells with different operating temperatures, electrolyte materials, power outputs, electrical efficiencies, and typical applications [14, 15].

1.1.1 Fuel cell types

One of the most common ways to classify fuel cells is by the type of electrolyte they use. Following this criterion, the following types can be distinguished:

- **Alkaline Fuel Cell (AFC):** This cell was one of the first modern fuel cells used. In general, H_2 is used as fuel and KOH or NaOH as electrolytes. One advantage of alkaline fuel cells is that at low temperatures, the activation overvoltage at the cathode is usually less than that in acid fuel cells. Additionally, because the cathode will be made from non-precious metals, the cost of the electrodes will be considerably lower than other types of fuel cells. Nevertheless, these fuel cells are easily poisoned with a small amount of CO_2 in the air [16, 12].

- **Proton Exchange Membrane Fuel Cell (PEMFC):** Also called, solid polymer fuel cell (SPFC), where its electrolyte is an ion exchange polymeric membrane. Water is the only liquid used by these cells; hence, the corrosive fluid hazards are minimal. For efficient performance, water management in the membrane is critical, and the polymer electrolytes work at lower temperatures to avoid the by-product water to evaporate faster than it is produced. Consequently, due to the low operating temperature, these fuel cells can start functioning faster than other fuel cells [17, 18].

- **Phosphoric Acid Fuel Cell (PAFC):** The electrolyte used is phosphoric acid. Its operating temperature is around 150 to 220 °C. At low temperatures, the phosphoric acid is a weak ionic conductor and can be easily poisoned by CO. Platinum dispersed on carbon-based supports is used as a catalyst on both sides of the cells [19, 9]. This fuel cell is the most used for stationary applications.

- **Molten Carbonate Fuel Cell (MCFC):** The electrolyte used in this fuel cell is a combination of alkali carbonates such as LiK or LiNa, which can be supported in a ceramic matrix of $LiAlO_2$. The average operating temperature is between 600 - 700 °C, allowing the alkali carbonates to form a highly conductive molten salt, where the CO_3^{2-} ions provide the ionic conduction. This type of fuel cell performs at high temperatures allowing non-precious metals to be used as electrocatalysts lowering its market value [20, 21].

- **Solid Oxide Fuel Cell (SOFC):** In these cells, solid oxide ion-conductive materials are employed as electrolytes, usually Y_2O_3 stabilized ZrO_2. The operating temperature of these cells is between 700 to 1000 °C, allowing the conversion of a wide range of fuels, including some hydrocarbon fuels. One of the disadvantages of this type of fuel cell is the high resistance due to the low electrolyte conductivity and some mass transport limitations due to the thickness of the anode or cathode [22, 23].

- **Direct Methanol Fuel Cell (DMFC):** This type of fuel cell has an advantage over (PEMFC) because methanol is a liquid with a relatively high density like without the need for external reforming [24]. Because the fuel is a liquid, DMFCs are easy to handle, store, transport, and simplifies the fuel cell system. Natural gas or renewable biomass sources can produce methanol, making it an accessible fuel [25, 26]. Besides, it was proven that the electro-oxidation of methanol improves in alkaline media [11], because of the oxidation reaction of methanol exhibits almost no sensitivity to the surface structure [27]. Furthermore, it reduces the cross over and risks of electrode materials, which are subject to corrosion, thus ensuring longevity [28].

  One of the essential aspects of this type of fuel cell is its MEA because it contains the catalyst, which plays an essential role in determining the fuel cell system's overall performance [15]. Moreover, the catalyst is required to bring the kinetics of the electrochemical reaction to a practical level [29]. Different electrode materials based on Pt and Pt-binary electrodes are used as electrocatalysts for

the electrochemical oxidation of methanol [30].

1.2   Electrocatalysis

The field of catalysis that studies reactions that involve charge transfer at the interface between a solid electrode and an electrolyte is electrocatalysis [31]. The rate of the electron transfer in an electrocatalytic reaction depends on the electrode material, which acts as an electrocatalyst. This is because the interaction of the electrode with certain species of the reaction, through adsorption, may decrease the activation energy of crucial reaction steps, accelerating the overall reaction rate. Considering that electrode reactions are heterogeneous, electrocatalysts are usually referred to as heterogeneous electrocatalysts [32]. The reactions of interest in fuel cell technology and water electrolysis, such as hydrogen evolution, oxygen evolution, and methanol oxidation, are electrocatalytic [33, 8]. Thus, a lot of effort has been devoted to the design of better electrocatalysts. The ideal electrocatalyst would be the one which complies with the following characteristics: high electrocatalytic activity, electrochemical stability, profitable price, and high abundance [6, 10].

For a better understanding of electrocatalysis some principles of electrochemistry must be discussed. By definition, an electrochemical cell is a device capable of producing electrical energy from chemical reactions (galvanic cells), or of producing a chemical transformation through the introduction of electrical energy (electrolytic cells) [34].

Electrochemical cells are composed of:

- **Electrolyte:** a substance that contains free ions and acts as an ionic conductor to ensure its conductivity.

- **Electrodes:** electronic conductors in contact with the electrolyte. The electronic transfers in an electrochemical cell take place at the electrode electrolyte interface.

  - Anode: electrode where the oxidation takes place.

$$\text{Red}_1 \rightarrow \text{Oxd}_1 + ne^- \tag{1.1}$$

  - Cathode: electrode where the reduction takes place.

$$\text{Oxd}_2 + ne^- \rightarrow \text{Red}_2 \tag{1.2}$$

Commonly, electrochemical phenomena are studied using a three-electrode cell arrangement, like the one shown in Fig 1.3. The working electrode (WE) is the electrode at which the redox processes under study occur. The current of the system flows between the WE and the counter (CE), whose only task is to complete the electrical circuit. To prevent any changes to the electrolyte composition, the CE is made of an inert material with a surface area significantly larger than the WE. Finally, the reference electrode (RE), made of a stable redox pair, has a constant and stable potential and is used to provide the potential on the working electrode with respect to that of the RE [35, 36].

The potential of an electrochemical reaction under thermodynamic equilibrium is described by the Nernst equation 1.3.

$$E = E^0 + \frac{2.303RT}{nF} \log \frac{C_O}{C_R} \tag{1.3}$$

where E^0 is the formal potential, R the gas constant, T the temperature, n is the number of electrons transferred, F is Faraday's constant, and C_O and C_R are the concentration of the oxidized and reduced species in solution. The change in Gibbs free energy of a chemical reaction and its relation to the cell's voltage can be described
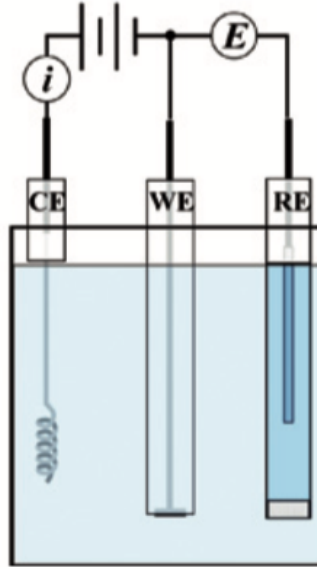
Figure 1.3: Schematic representation of three electrode electrochemical cell: working electrode (WE), reference electrode (RE) and counter electrode (CE). Taken from[7].

in the next equation [37]:

$$\Delta G = -nFE \tag{1.4}$$

where E is the voltage of the redox-pair in thermodynamic equilibrium.

When a potential difference is applied between the WE ad RE using an external power source, a current flows through working and counter electrodes [9]. The difference between the equilibrium potential (E_{eq}) and the potential applied is known as an overpotential (see equation 1.5).

$$\eta = E - E_{\mathrm{eq}} \tag{1.5}$$

The Butler–Volmer equation 1.6 [35, 36] describes the relation between the current density, j, and the overpotential, η

$$j = j_o \left[\exp \left(\frac{\alpha n F \eta}{RT} - \frac{(1-\alpha)nF\eta}{RT} \right) \right] \tag{1.6}$$

where j_0 is the exchange current density and α the transfer coefficient. The two terms

in the equation represent the cathodic and anodic components of j. Thus, at $\eta < 0$, the reaction proceeds in the cathodic (reduction) direction, while $\eta > 0$ favors the anodic (oxidation) reaction. The best performance of an electrocatalyst is obtained when high current densities are obtained at low overpotentials [32].

1.2.1 Adsorption

As mentioned earlier, adsorption is a fundamental step in electrocatalytic reactions. According to the Sabatier's principle [38], an ideal electrocatalyst adsorbs a chemical species with just enough strength, i.e., not too weakly as to activate the through a binding interaction, and not too strongly to ensure the desorption of the intermediates or products. When the activity of a series of electrocatalysts is plotted against adsorption energy a *volcano plot* is produced.

Figure 1.4 shows the volcano plot for Hydrogen Evolution Reaction, one of the most studied electrocatalytic reactions due to its simplicity [39]. The H adsorption free energy controls the catalytic activity. The metals located to the left side of the maximum present weak binding energies towards H; therefore, their catalytic activity is low since they do not adsorb hydrogen with sufficient affinity to carry out the reaction efficiently. On the other hand, metals located to the right of the maximum have very high binding energies resulting in inefficient desorption of hydrogen [40]. In this series, platinum has the optimum binding strength, allowing the reaction of interest to be carried out. Platinum is also known to be the best catalyst for the methanol oxidation reaction (MOR).

1.2.2 Electrocatalytic properties of nanoparticles

Despite the outstanding performance of platinum as electrocatalyst, its high cost and scarcity has limited the expansion of fuel cells. Therefore, it is beneficial to reduce
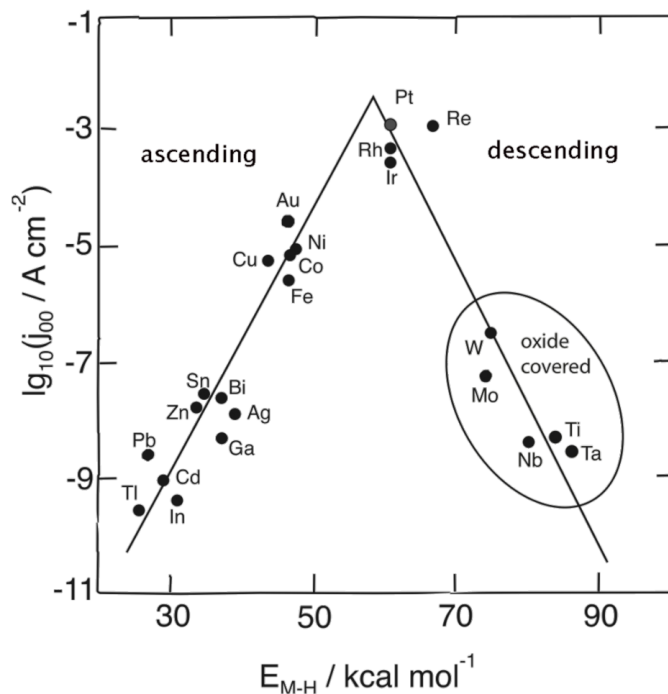
Figure 1.4: Volcano plot for the Hydrogen Evolution Reaction in acidic solutions. Taken from [40].

the catalyst particle size because this increases significantly the active surface area, allowing for more active catalytic sites per unit of mass [39].

Electrocatalysis is one of the fields of most extensive application of nanoparticles. Metal nanoparticles present physical and chemical properties such as chemical reactivity, optical and electronic properties, size, and shape-dependent interatomic bond distances, which can differ significantly from those of the bulk material [28]. Nanoparticles can improve the intrinsic properties of the material and can be designed to achieve a particular functionality due to the following characteristics:

- **Particle size effect:** In electrochemistry, fuel-cell reactions are among the most studied electrocatalytic reactions, where the electrocatalysts are responsible for providing their best efficiency. Fuel cell efficiency can be evaluated by measuring the current density drawn at an overpotential, j (ampere/projected electrode surface area) [41], as expressed by equation 1.7

$$j/\,\mathrm{A\,cm^{-2}} = j_s/\mathrm{A\,cm^{-2}} \times s/\mathrm{cm^2\,g^{-1}} \times w/\mathrm{g\,cm^{-2}} \qquad (1.7)$$

composed of three important factors: i) the specific current density j_s (amperes/electroactive surface area); ii) the specific surface area of catalyst s (electroactive surface area/g), and; iii) the amount of loaded catalyst w (g/projected electrode surface area). When noble metals are employed as electrocatalysts, such as platinum, it makes more economic sense to increase the specific surface area s and keep the mass w constant.

An example of the particle size effect is given by Oberbury et al. [42]; where they showed that, although macroscopic gold is inert for CO oxidation, gold nanoparticles with 2 to 5 nm in diameter are excellent catalysts for this reaction. They concluded that lower coordination sites present on the surface of the nanoparticles provide more stable adsorption sites and thus are more reactive. They also suggested that such dependence can apply if only corner-type sites on Au particles contribute to the activity. As shown in Figure 1.5, there is an inversely proportional relationship between particle size and catalytic activity.

- **Effect of particle shape and surface structure:** Synthesis of shape-selected nanoparticles, with specific surface facets exposed, can be used to tailor the catalytic activity of the particles towards certain reactions. Hao et al. [43] reported the influence of the shape on the catalytic activity for methanol oxidation in alkaline media, where cubic Pd nanocrystals (7 nm) exhibited much better catalytic activity (in terms of overpotential and significant current response) because they contained more {100} facets than the spherical nanocrystals. This shape-dependent activity can be attributed to fact that certain geometries give the right surface structure (Miller indices) for better catalytic activity. Atoms with low coordination number tend to be more reactive; thus, different shapes would have a different concentration of under-coordinated atoms, and therefore different activity.
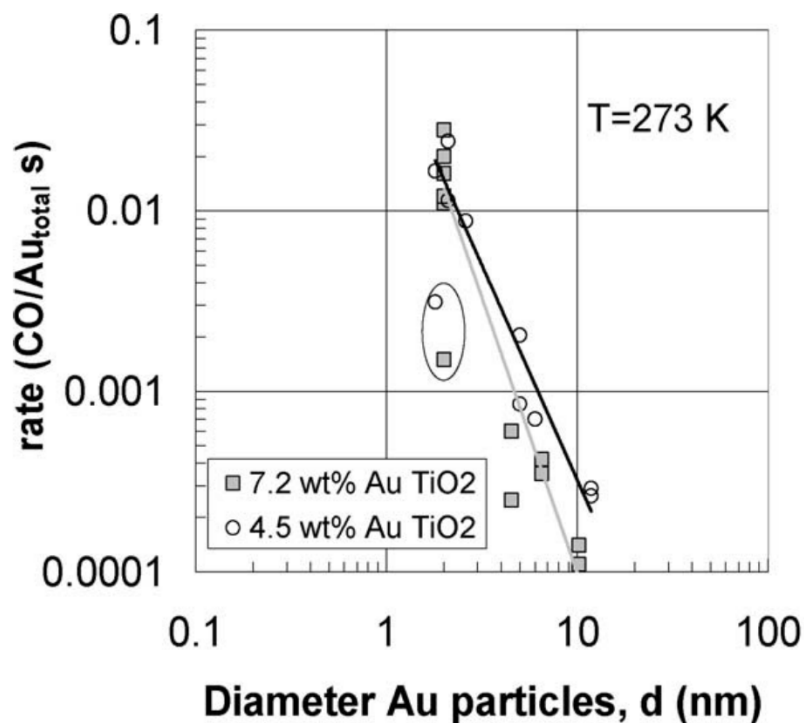
Figure 1.5: Study of size-effect of gold nanoparticles (3–5 nm) on the catalytic properties of CO Oxidation. Taken from [42].

Catalytic activity can also be enhanced by using metal nanofilms instead of nanoparticles. A nanofilm is defined as a thin layer of metal spanning from a fraction of a nanometer to several micrometers in thickness. Thin films' particle density is increased to a point where even the coalescence thickness of the particles is in the subnanometer regime, improving the electronic transfer because of the closer contact between the substrate's surface and the nanofilm.

In previous works, the use of thin films improved electrocatalytic activity. One example is given by Liao et al. [44] for hydrogen evolution reaction. They showed that the best catalytic activity was obtained with Au (111) supported Pt monolayers than Pt (111). This is due to the fact that a Pt film has a larger interatomic spacing and is two times more active than that bulk Pt (111). Another example is given by Feng et al. [45], who demonstrated that the hydrogen evolution reaction and oxygen evolution reaction were improved with the use of Ni_3S_2 over nanosheets on nickel foam (NF) rather than the use of Ni_3S_2 nanoparticles. Figure 1.6 shows that Ni_3S_2/NF

exhibits a remarkable catalytic activity towards hydrogen evolution reaction, much higher than that of Ni_3S_2 nanoparticles. This is because, Ni_3S_2/ NF's have much higher electrochemical surface area ($187.5cm^2$) than that of Ni_3S_2 nanoparticles. Besides, the intimate contact between Ni_3S_2 nanosheets and nickel foam (the support material) facilitates interfacial electron transport between the two. That was supported by electrochemical impedance analysis, where the results show that Ni_3S_2/NF has a much lower faradaic impedance value than Ni_3S_2-NP, indicating that the electron transfer rates during hydrogen evolution reaction are much faster for Ni_3S_2 film on NF than for nanoparticles.
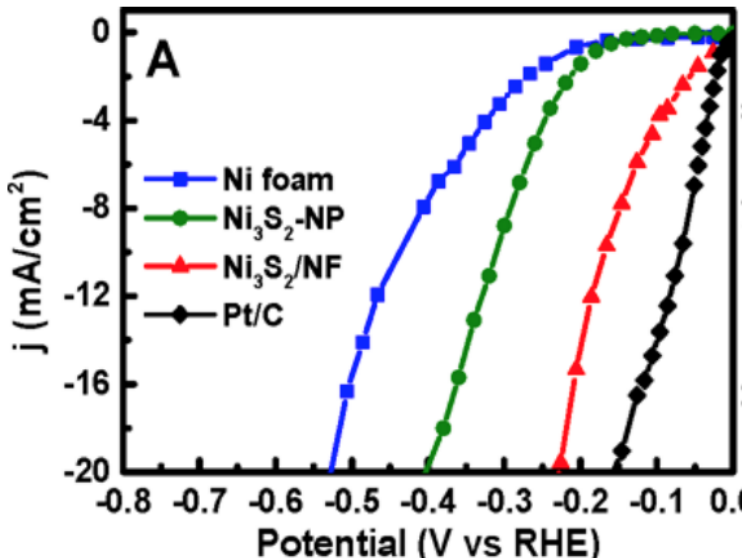
Figure 1.6: Steady-state current density as a function of applied voltage during HER at pH 7 over nickel foam (NF), Ni_3S_2 nanoparticles, Ni_3S_2/NF, and Pt/C (20 %wt). Taken from [45]

1.3 Electrodepostion of Electrocatalysts

The studies presented in the previous section evidence the advantages of catalytic activity of thin films over nanoparticles. For these reason, in the present work, nickel thin-films were produced by short galvanostatic pulse as electrocatalysts for methanol

electro-oxidation.

Among the available methods for electrocatalyst fabrication, electrodeposition stands out as a simple, fast, low cost, versatile, and easy to control method. Electrodeposition consists on the electrochemical formation of a new phase over a substrate, which acts as a substrate. The morphology of the deposits can be tuned by controlling the composition of the electrolyte, the applied potential, or the applied current. Although in most cases the substrate is a material with low electrocatalytic activity for the reaction of interest, interaction with the electrocatalyst may have an important effect on the activity of the electrode.

The electrodeposition process consists of the following three stages [46]:

a) Formation of metal adatoms on the substrate,

b) Two-dimensional (2D) and three dimensional (3D) metal phase formation via nucleation and clusters growth,

c) Crystal growth of the 3D metal bulk phase.

Two significant factors need to be in consideration for the metal electrodeposition process: i) thermodynamics and growth properties of (2D) and (3D), ii) the properties of the electrolyte phase that strongly affects the structure of the substrate, the kinetics of the mass and charge transfer across it.

To start the electrodeposition process a nucleation overpotential must be surpassed. This value is defined by Guo et al. [47] as the potential corresponding to the onset of the reaction $M^+ + S + e^- \rightarrow M - S$ referenced to the equilibrium potential for M^+/M couple at a site S. Budevski et al.[48] explained that metal electrodeposition generally follows the Butler-Volmer kinetics (equation 1.6). Once the nucleation overpotential is surpassed, the cations that reach the electrode surface are discharged and adsorbed on it, forming metal adatoms (M–S). These adatoms group to form clusters (nuclei), which grow under diffusion control to form isolated particles or continuous films.

Electrodeposition can be produced either through potential control (potentiostatic method) or current control (galvanostatic method). In the former, the Gibbs energy of the systems is controlled by the applied potential, defining the electrodeposition kinetics. In contrast, galvanostatic electrodeposition consists on applying a fixed current to the system, imposing the electrocrystallization kinetics. In response, the working electrode adjusts its potential to a value at which the electrodeposition process is capable of supplying the imposed charge transfer [46]. Videa et al. [49] reported the use of short galvanostatic pulses for the electrodeposition of nickel nanoparticles in indium tin oxide (ITO) as substrate. They concluded that this method led to a smaller dispersion in the particle size and greater growth control of the nuclei.

1.3.1 Galvanostatic Electrodeposition

This technique has been widely used in industrial applications. However, fundamental understanding of this method is complicated by the fact that nucleation and growth happen under variable overpotential conditions. Isaev et al. [46, 50] developed a theory of galvanostatic phase formation. They considered 1) the charge of the double layer, 2) the discharge of depositing ions and accumulation of adatoms on the electrode, 3) the overpotential dependences of nucleation rate and growth rate of clusters, and 4) the mass consumption of the precursor by diffusional growth of clusters during the phase formation.

The behaviour of the potential during an galvanostatic electrodeposition will be illustrated by Figure 1.7:

The first region occurs within the first ten milliseconds after the current pulse is applied; the electrode experiences a potential drop, reaching values negative to the onset of hydrogen evolution reaction (HER) on gold (–0.70 V vs. MMSE from cyclic voltammetry measurements). During the next regime (II), the potential shows a slow recovery. In agreement with Isaev et al. [46], and Videa et al. [49], these stages
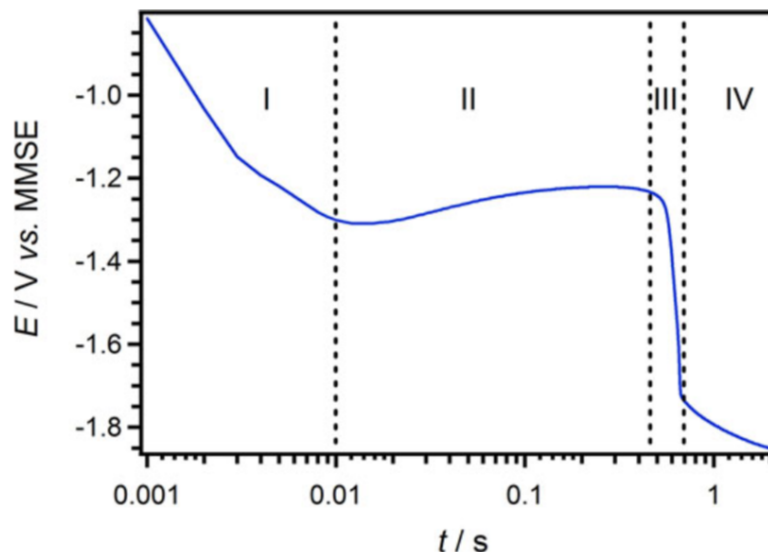
Figure 1.7: Typical potential transient recorded during a galvanostatic deposition of Ni on a clean Au electrode. A logarithmic timescale was used. Taken from [51].

were assigned to the nucleation and growth of the Ni deposit. They are followed by a significant drop in potential (regime III) indicating the depletion of the precursor and then, a progressive polarization towards more negative potentials in regime IV. These stages correspond to the end on Ni deposition and the start of water reduction.

As shown in Figure 1.8, the minimum potential value on regime (I) depends on the current pulse magnitude, the more intense the applied current the lower potential values, which are reached in shorter times. In contrast, the potential of regime (II) is almost independent of the applied current, unlike its duration. Larger currents lead to shorter times in regime (II).

1.3.2 Self-terminated Electrodeposition

During electrodeposition reactions, nucleation and growth are followed by electrolyte reduction that may affect properties of the electrodeposit such as morphology, microstructure and chemical composition of the deposit. The overall current efficiency of electrodeposition of iron groups elements (Fe, Co, Ni) [52], can be affected by the
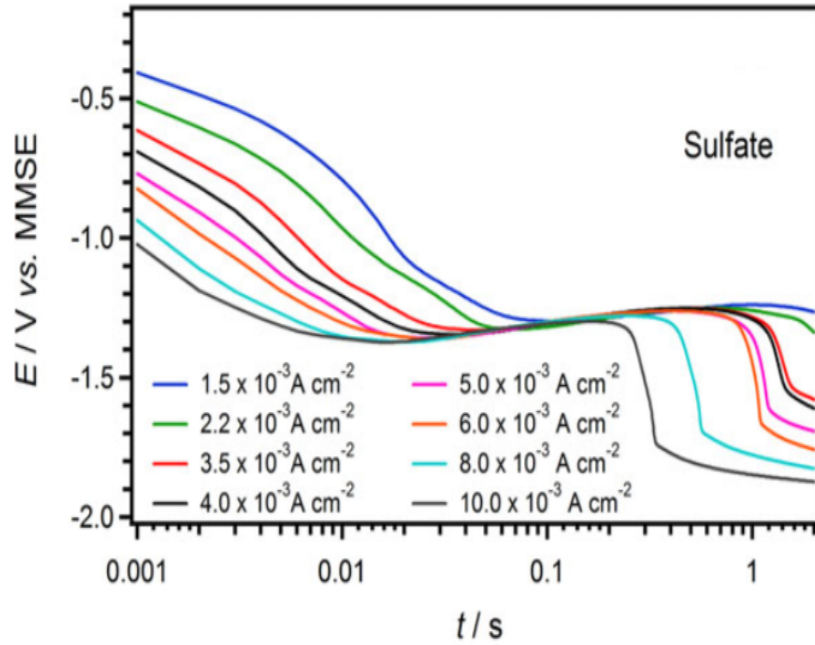
Figure 1.8: Potential transients recorded during galvanostatic deposition of nickel on a clean Au electrode at different applied currents pulses. Plating bath: 50 mM NiSO$_4$ + 500 mM Na$_2$SO$_4$. Taken from [51]

Hydrogen Evolution Reaction, shown in the equations 1.8 and 1.9:

$$2\,H_3O^+ + 2\,e^- \rightarrow H_2 + 2\,H_2O \qquad (1.8)$$

$$2\,H_2O + 2\,e^- \rightarrow H_2 + 2\,OH^- \qquad (1.9)$$
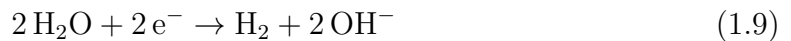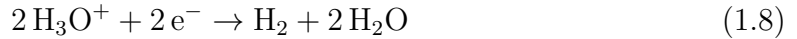
One of these effects is self-termination electrodeposition, which can be defined as the quenching of the metal deposition caused by interaction with an electrolyte breakdown processes, which takes place at high overpotentials. For example, Pt electrodeposition at high overpotentials can lead to the formation of thin films, since hydrogen adsorption on the newly formed Pt terminates the deposition [53]. Another self-termination mechanism is observed for Fe-group metals (Ni, Co, Fe) electrodeposition. At potentials negative to the onset of water reduction, OH$^-$ generation leads to the formation of a hydroxide monolayer that blocks the electrodeposition [52]. Moffat et al. [54, 52]

reported that self-terminated electrodeposition enables effective deposition of ultra-thin films. Additionally, they studied the self-termination of nickel deposition on gold microelectrodes, as shown in Figure1.9. An unusual voltammetric spike was observed around -1.46 V (vs Ag/AgCl) near the onset of H_2O reduction, that can be correlated with the self-termination of Ni deposition. The current spike is due to autocatalytic H_2 evolution, which is related to the nucleation and growth of a thin nickel hydroxide layer. In the reverse sweep, the anodic wave at -0.15 V (vs Ag|AgCl) corresponds to stripping of the Ni film and any incorporated H.
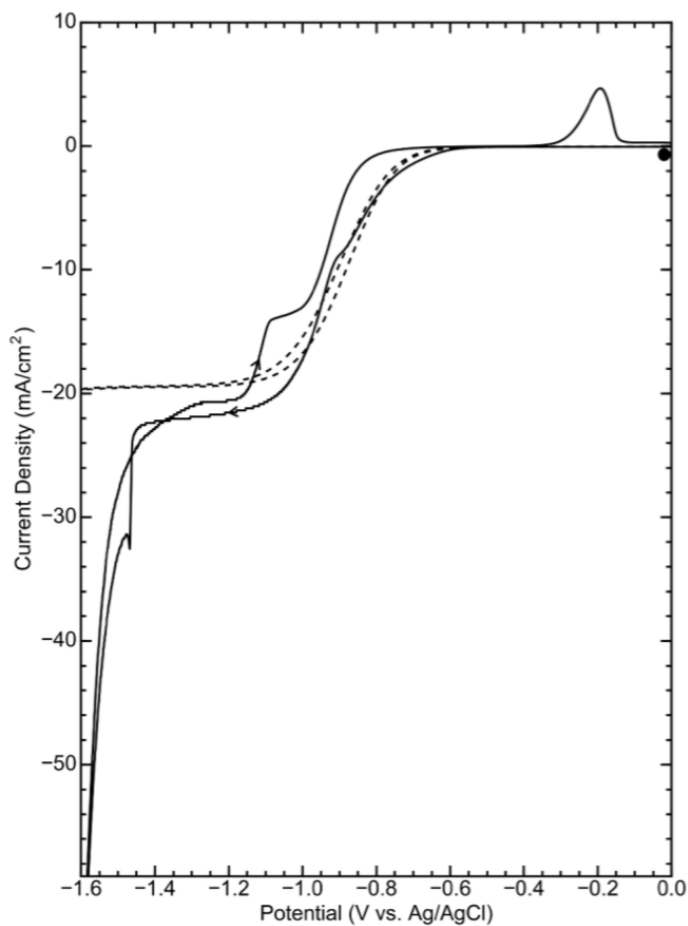
Figure 1.9: Cyclic voltammetry of an Au ultramicroelectrode in 5.0 mM NiSO$_4$ + 0.05 M Na$_2$SO$_4$ pH 3.0. Dashed line is supporting electrolyte. Sweep rate, 20 mV/s; initial potential, 0.00 V; anodic potential limit, 0.00 V; electrode radius, 12.5 μm. D_{Ni} = 5.8×10^{-6} cm^2 s^{-1}; current efficiency at -1.20 V was $23\pm11\%$; charge in current spike was 8.8 ± 1.2 mC cm^{-2}. Taken from [54].

During galvanostatic electrodeposition, the potential is freely adjusted, thus the possibility of self-termination must be taken into account to analyse the results of Pt and Fe-group metal electrodeposition.

1.4 Methanol Oxidation Reaction (MOR)

Direct methanol fuel cells are considered a promising power conversion alternative because of their characteristics in terms of reactivity at low temperatures, storage, the high theoretical energy density (6100 $Whkg^{-1}$ at 25°C) [55].

DMFCs generate electrical work from the oxidation of methanol and the reduction of oxygen. The reaction occurring on the anode is given by:

$$CH_3OH + 6\,OH^- \rightarrow 5\,H_2O + CO_2 + 6\,e^- \tag{1.10}$$

The carbon dioxide generated from the oxidation reaction is removed by the flow of the methanol's aqueous solution. At the cathode, the O_2 is fed into the cell and undergoes the following reaction [5]. :

$$\frac{3}{2}\,O_2 + 3\,H_2O + 6\,e^- \rightarrow 6\,OH^- \tag{1.11}$$

The overall cell reaction is shown in equation 1.12. Therefore, the complete oxidation of methanol to CO_2 requires six electrons [56, 28].

$$CH_3OH + \frac{3}{2}\,O_2 \rightarrow CO_2 + 2\,H_2O \tag{1.12}$$
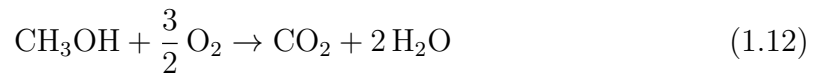
The thermodynamic cell potential is 1.2 V; hence it is complex and does not occur in a single reaction [57].

As mentioned in section 1.1, one of the fundamental components in a fuel cell is

the electrocatalyst since it determines the efficiency and rate of the reaction. One of the goals in the present work is to study the methanol oxidation reaction on the nickel deposits produced. Electro-oxidation of methanol proceeds through a multistep reaction and its mechanism will be described next.

1.4.1 Mechanism of MOR and kinetics of the anodic reduction of methanol

Early works like Tritsaris and Iwasita [58, 59] have studied the methanol oxidation mechanism in acidic media. Tritsaris proposed that methanol oxidation proceeds through the following indirect paths:

$$CH_3OH \rightarrow CO + 4\,(H^+ + e^-) \tag{1.13}$$

$$H_2O \rightarrow OH + (H^+ + e^-) \tag{1.14}$$

$$CO + OH \rightarrow CO_2 + (H^+ + e^-) \tag{1.15}$$
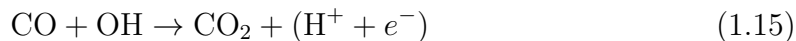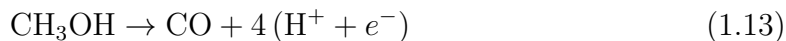
The oxidation of methanol to adsorbed CO is described in equation 1.13. Equation 1.14 represents the activation of water to form adsorbed OH, and equation 1.15 describes the combination of both adsorbed species to form the final reaction product, CO_2.

However, methanol oxidation in alkaline media proceed in through a different mechanism and has some advantages over acid media such as [60]:

- Catalytic activity of both noble and non-noble metals to produce the electrocatalysts.

- Improves the kinetics of the ORR and alcohol oxidation reaction. This is partly

due to the hydroxyls in alkaline media further facilitate the methanol dehydrogenation process and the oxidation removal of CO species during the MOR [61].

- Reduced alcohol crossover by electro-osmotic drag of hydroxyl ions.

- Reduced risk of corrosion of the cell materials.

It is generally accepted that the MOR mechanism undergoes two parallel paths: a) the "direct" or "active intermediate" path, which proceeds via the oxidation of methanol directly to CO_2 without the formation of metal-poisoning intermediates such as CO, and b) the "indirect" or "poisoning intermediate" path, which involves the production of poisoning species. These pathways are shown in Fig. 1.10. Tritsaris et al. [58]
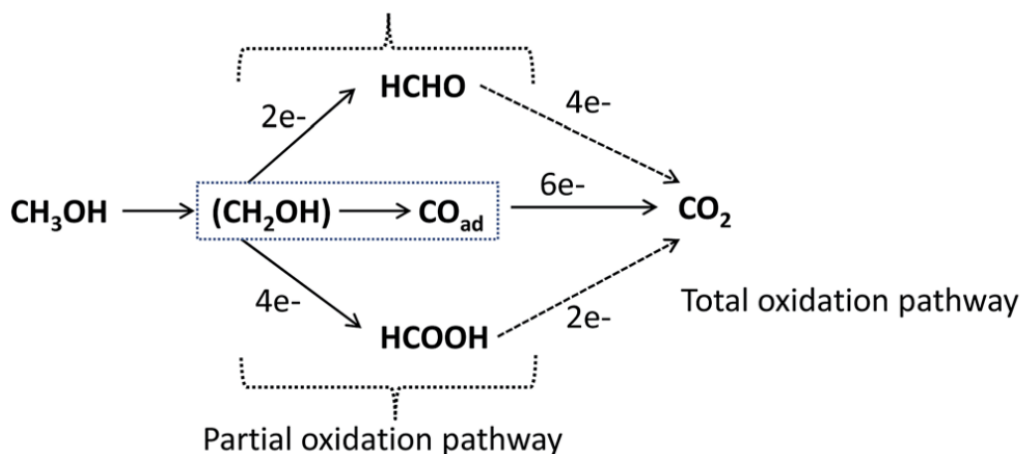
Figure 1.10: Schematic of the parallel pathways for the electrocatalytic oxidation of methanol. Taken from [28].

elaborated a volcano plot for methanol oxidation reaction according to the surface-specific values of the binding energies of CO ΔG_{CO} and OH ΔG_{OH}, as shown in Figure 1.11. The volcano plot is separated into three distinct regions, each corresponding to a different potential-determining step (Eq. 1.13, Eq. 1.14, Eq. 1.15). The higher in energy the d-band center lies, the stronger the interaction between the surface and the adsorbate. Therefore, undercoordinated atoms will bind OH and CO strongly.

On the lower left part of the volcano plot, lie the metals with the flat surfaces that are expected to have lower overpotentials. In contrast, the metals that lie on the upper right part of the volcano plot, are expected to have lower overpotentials and are estimated for the respective stepped surfaces, due to the ability to dissociate absorbing molecules [62]. They determined that for an efficient catalyst, the potentials for U_{CO}, U_{OH}, and U_{CO_2} that correspond to potential-determining steps will be equal to each other, and for the ideal catalyst, all three will be equal to zero. Plat-
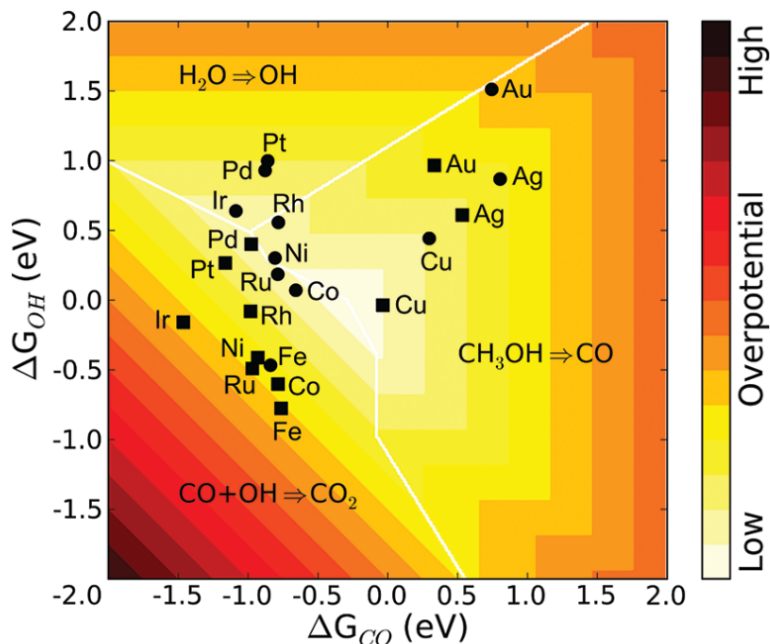
Figure 1.11: Volcano plot for the indirect path, for stepped surfaces (squares) and flat surfaces (circles). The overpotential minimizes over an area (white) of optimal CO and OH adsorption energies. Taken from [58].

inum in comparison with the other metals, is considered one of the best catalysts for methanol oxidation reaction because it shows the lowest possible value for the overpotential [61]. As discussed in the section 1.2.2, the high cost and limited resources of Pt enormously restrict its application [4]. In alkaline media, the electro-oxidation of methanol is more efficient, because the bonding of chemisorbed intermediates appears weaker than in acidic media [63]. Nickel has received greater attention, not only because of its accessible price, but also because of its significant performance in

the electrocatalytic oxidation of methanol, as Guo et al. [64] reported by depositing nickel nanoparticles on indium tin oxide (ITO) electrodes. Similarly, Rahim et al. [65] noticed a significant performance toward methanol oxidation, when sheets of nickel were deposited in graphite electrodes.

Nickel redox sites have shown high catalytic activity towards the oxidation of small organic compounds such as methanol in alkaline media. Golikand et al. [66] proposed a mechanism for methanol electro-oxidation on Ni, where they did not consider temperature variation:

$$Ni(OH)_2 + OH^- \rightleftharpoons NiOOH + H_2O + e^- \tag{1.16}$$

$$CH_3OH + NiOOH \rightarrow NiOOH(CH_3OH)_{ads} \tag{1.17}$$

$$NiOOH(CH_3OH)_{ads} + NiOOH \rightarrow NiO + NiOOH(CH_3OH)_{ads} + H_2O \tag{1.18}$$

$$NiOOH(CH_3OH)_{ads} + NiOOH \rightarrow NiO + NiOOH(\dot{C}OH)_{ads} + H_2O \tag{1.19}$$

$$NiOOH(\dot{C}OH)_{ads} + OH^- \rightarrow NiO + HCOO^- + H_2O \tag{1.20}$$
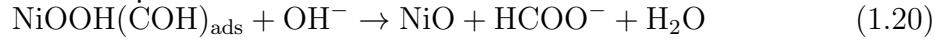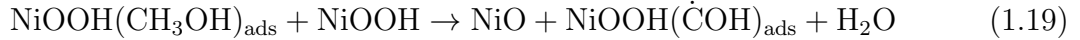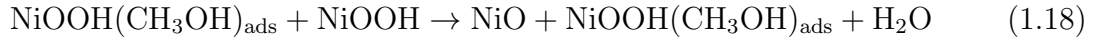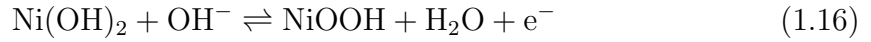
The adsorption energies of all of the methanol oxidation reaction intermediates binding through a O and C atoms are shown in Fig. 1.12.

By using the established linear relationships, the binding free energies of the MOR intermediates can be expressed as functions of ΔG_{CO} and ΔG_{OH}. For example, the adsorption energy of HCOOH is calculated as $\Delta G_{HCOOH} = 0.97 \; \Delta G_{OH} + 0.81$ eV. Effectively, the reaction overpotential can be estimated for a pair of (ΔG_{CO}, ΔG_{OH}) energies.

1.5 Hypothesis

From all that was previously presented, the working hypothesis for this research is enunciated as follows:
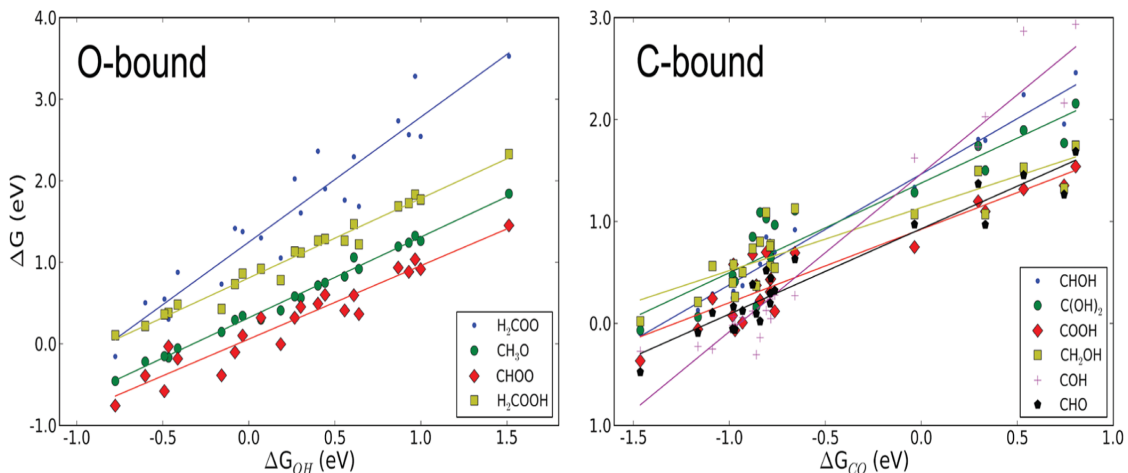
Figure 1.12: Linear relationships between the adsorption free energies of methanol oxidation reaction intermediates and the adsorption energy of OH (left) or CO (right), for O- or C-bound species, respectively. Taken from [58].

By controlling the nickel galvanostatic electrodeposition gold substrate through the parameters: i) pulse duration and ii) pulse density a nickel deposit with efficient electrocatalytic activity towards methanol oxidation can be produced.

1.6   Objectives

The general objective of the present project is to synthesize thin nickel films by the use of the galvanostatic method and to study the effect of the experimental parameters selected on is electrocatalytic activity for the methanol oxidation reaction.

To achieve this goal, the specific objectives were:

- Study the self-terminated nickel electrodeposition using microelectrodes in order to acquire a better understanding of the nickel electrodeposition mechanism.

- Study the surface activation effect of nickel films through a repeated oxidation

process to efficiently convert the deposited Ni into the active form $Ni(OH)_2$.

- Interpret form the electrochemical characterization (cyclic voltammetry and sample current voltammetry) the polymorph structures of $Ni(OH)_2$ obtained after their surface activation.

- Study the relation between the $Ni(OH)_2$ polymorphs and their oxidation into the active NiOOH structure in the electrocatalysis of the methanol oxidation reaction.

- Select the experimental parameters that lead to the deposit with the highest electrocatalytic activity for the oxidation of methanol.

Chapter 2

Experimental Methodology

In this chapter, the general procedures followed for the experimental part of this work will be described in detail.

2.1 Electrochemical cell

All experiments were carried out in a single compartment, three-electrode cell, placed inside a grounded Faraday cage to minimize external electrical interferences. Electrochemical experiments with microelectrodes were performed using a PC controlled PGSTAT101 Autolab, while experiments with macroelectrodes were executed using a CH Instruments Model 700D Potentiostat/Galvanostat. Figure 2.1 shows the elements in the electrochemical setup.

a) Two types of electrochemical cells were employed: a) glass cells of either $10\,\mathrm{mL}$ or $120\,\mathrm{mL}$, for neutral or acidic electrolytic baths. b) A Teflon cell with a volume of $80\,\mathrm{mL}$ was used to contain potassium and sodium hydroxide alkaline solutions. All cells were furnished with a lid allowing the electrodes to be fixed in position and to accommodate for purge gas inlet and outlet.
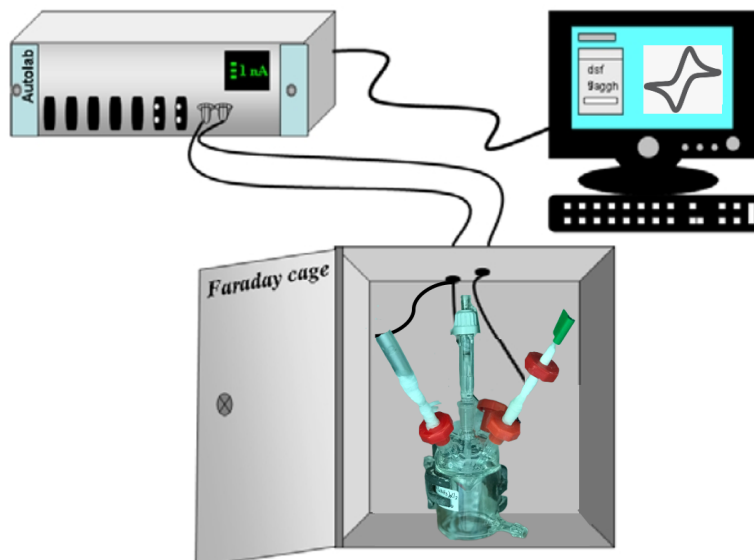
Figure 2.1: Schematic representation of Potentiostat/Galvanostat PGSTAT101 Autolab and the three-electrode electrolytic cell arrangement. Edited from [67].

b) A Pt mesh or Pt coiled wire (geometric area of $\sim 3.3\,\mathrm{cm}^2$) served as counter or auxiliary electrodes.

c) Ni wire with diameters of $25\,\mu$m and $500\,\mu$m and Au wires with diameters of $50\,\mu$m and $500\,\mu$m were used to buid the working electrodes.

d) A reference electrode. Different reference electrodes used depending on the electrolyte:

- Mercury-mercury sulfate reference electrode (MMSE). $\mathrm{Hg}|\mathrm{Hg_2SO_4}$ (0.650 V vs NHE) in saturated solution $\mathrm{K_2SO_4}$. The electrode $\mathrm{Hg}|\mathrm{Hg_2SO_4}$ consists of a paste of metallic mercury and mercury (I) sulfate ($\mathrm{Hg_2SO_4}$). This electrode has excellent reproducibility [34]. Its half-cell redox reaction is:

$$\mathrm{Hg_2SO_4\,_{(s)} + 2\,e^- \rightleftharpoons 2\,Hg\,_{(l)} + SO_4^{2-}\,_{(ac)}} \qquad (2.1)$$
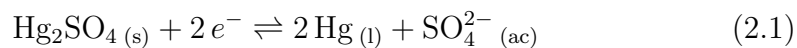
- Silver-silver chloride electrode: $\mathrm{Ag}|\mathrm{AgCl}$ (0.198 V vs. NHE) in a saturated

27

KCl solution. Equation(2.2) corresponds to its half-cell reaction is:

$$AgCl_{(s)} + e^- \rightleftharpoons Ag_{(s)} + Cl^-_{(ac)} \tag{2.2}$$
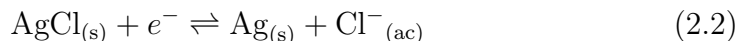
- Reversible hydrogen electrode (RHE): is a subtype of the standard hydrogen electrodes, with the only difference that its measured potential does change with the pH. The electrode potential for hydrogen E_{H2} can be determined with the following equation:

$$E_{H^+/H_2} = E^\circ_{H^+/H_2} + \frac{2.303RT}{nF} \log \frac{(a_{H^+})^2}{(P_{H_2})} \tag{2.3}$$

where a_{H^+} is activity of hydrogen ions, and P_{H_2} is hydrogen partial pressure.

2.1.1 Construction of the working electrodes

The working electrodes used in this project were build to study different characteristics of the electrochemical systems. For this purpose, macro- and microelectrodes were utilized and their construction procedure is described below:

Macroelectrodes

Nickel and gold macroelectrodes were made using a 0.5 mm diameter wire. The wire was electrically connected to a copper wire with indium for the Au electrode, or lead-tin solder for the Ni electrodes. The wires were sealed in epoxy resin, leaving only a disk cross-section exposed to the electrolyte as shown in Figure 2.2.

Microelectrodes

The working microelectrodes were made from gold wire of 50 μm diameters, sealed in a glass tube. A section 2 cm long gold wire was inserted into a 10 cm long Pyrex glass
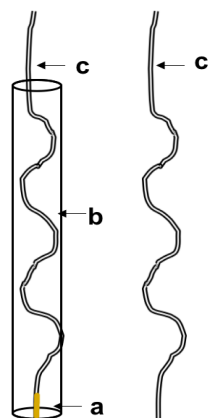
Figure 2.2: Schematic representation of the working macroelectrode has its specific parts: a) gold wire, b) epoxy resin, and c) copper wire.

drawn to a capillary end. Before inserting the fine wire, the glass capillary was first sealed at one end using a Bunsen burner, and the open end of the tube was connected to a vacuum line and the gold wire was sealed as represented in Figure 2.3.
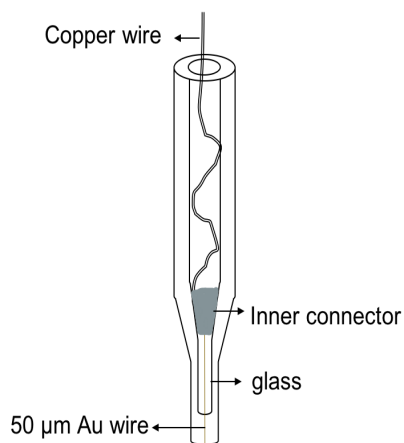
Figure 2.3: Schematic representation of the shielded 50 μm diameter Au microelectrode.

2.2 Conditioning of the working electrodes

Previous to the use of the working these were subjected to the following conditiong treatment:

2.2.1 Polishing of working electrode

Microelectrodes

After the microelectrode fabrication, each one was grounded on a polishing wheel with wet SiC paper of finer grades (240, 600, and 1200). Since these procedure leaves deep scratches and grooves, the microelectrodes were then subjected a second polishing stage with particles aluminum oxide (Buehler Ltd) paste of 5, 1, and 0.3 μm particle sizes. For better results, the microelectrodes were gently polished while being pressed perpendicular to a polishing cloth. The microelectrodes were sonicated in ultrapure water between each polishing step, to remove any attached particles. Finally, inspection under an optical microscope revealed a "mirror finish" surface.

Macroelectrodes

The gold electrodes were polished with alumina of particle sizes of 1, 0.3, and 0.1 μm; for 20, 12, and 10 minutes, respectively. In between each polishing step, the electrodes were rinsed with deionized water and cleaned by immersion in an ultrasound bath (1510 Branson) in propanol, acetone, and ethanol (G/R) for 3 minutes to obtain a mirror-like surface. Nickel electrodes were polished and cleaned following the same procedure. To remove nickel oxides from the electrode surface, the nickel electrode was immersed in 0.5 M sulfuric acid for 10 minutes.

2.2.2 Electrochemical cleaning and electrode conditioning

Cyclic voltammetry technique was used to remove impurities adsorbed on the working electrode surface. The electrolytic cell was assembled as shown in Figure 2.4, using Hg|Hg$_2$SO$_4$ as the reference electrode. The electrolyte used was 50 mM H$_2$SO$_4$ (Fermont, Trace ppb) for macroelectrodes and 1 M H$_2$SO$_4$ (BDH) for microelectrodes. For macroelectrodes, the cell was polarized from -0.8 to 1.06 V at a scan rate of 200 mV s^{-1} during the first 30 cycles, 100 mV s^{-1} for the next 20 cycles and 50 mV s^{-1} during the last 10 cycles. On the other hand, for microelectrodes, the electrode was polarized from -0.6 V to 1.2 V at a scan rate of 200 mV s^{-1} during 30 cycles. The cycling was stopped once a reproducible voltammogram was obtained and just after the peak corresponding to the reduction of gold oxide, to ensure a surface free of oxides.

Macroscopic nickel electrodes were not subjected to any electrochemcial cleaning.

Figure 2.4: Single compartment three-electrode cell.

2.2.3 Electroactive surface area of gold electrodes

Cyclic voltammetry was used to determine the electrochemical surface area (ECSA) of the gold electrodes. I was estimated by dividing the charge of the reduction of the oxide monolayer, corresponding to the area under the reduction peak as shown in Figure 2.5, by a constant of 390 μC cm^{-2} [68].
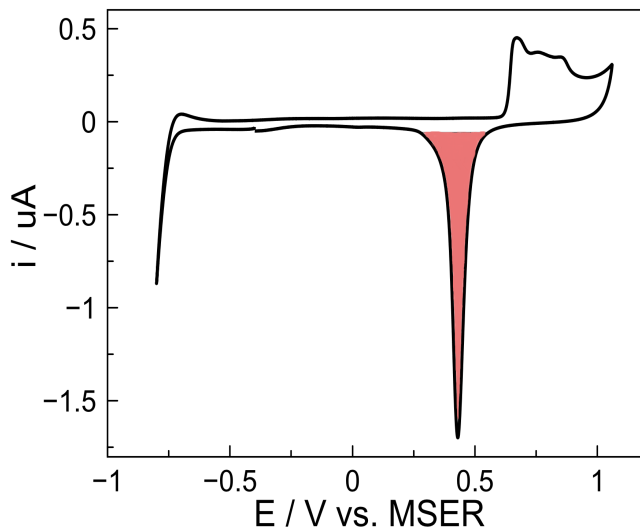
Figure 2.5: Typical voltammogram for a gold electrode at 50 mM H_2SO_4 at a sweep rate of 50 mV s^{-1}. The shaded area represents the reduction charge of the surface oxide formed during the anodic sweep.

The average value of the ECSA from six experiments was 10.0×10^{-3} cm^2, with a standard deviation of 3.6×10^{-3} cm^2. Normalized voltammograms show qualitative variations among the different electrodes (see Fig. 2.6), indicating that the surface conditions are not identical.
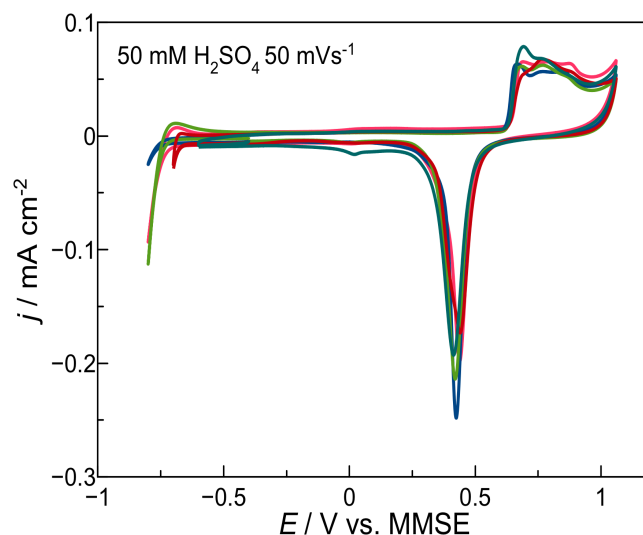
Figure 2.6: Six voltammograms normalized to the real surface area of the working electrode in 50 mM H_2SO_4 electrolyte at a sweep speed of $50\,mVs^{-1}$ after 60 stabilization cycles.

2.3 Electrochemical experiments

2.3.1 Electrodeposition of Nickel

Nickel electrodeposition experiments had different purposes. The research aims are to understand the nickel electrodeposition mechanism and to explore the galvanostatic method for controlled electrodeposition, using pulsed current experiments instead of double pulsed potential experiments.

2.3.2 Self-terminating electrodeposition of nickel on gold microelectrodes

The self-terminated electrodeposition on a Au microelectrode (50 μm diameter) was studied by cyclic voltammetry. Two different electrolytes were employed: 5 mM $NiSO_4 \cdot 6H_2O$ (Sigma Aldrich, 99%) + 100 mM Na_2SO_4 (CTR Scientific, 99.9%)

33

at pHs 2.69 (adjusted with H$_2$SO4) and 5 mM NiCl$_2 \cdot$6H$_2$O + 5 mM NaCl (CTR Scientific, 99.9%) at pHs 3.0 (adjusted with HCl). The effect of the reversal potential on the deposition was evaluated using two different values: limits -1.6 and -1.9 V vs Hg|Hg$_2$SO$_4$. The potential was swept from -0.5 V to -1.6 V or -1.9 V. In order to strip off the Ni film and any incorporated H, the potential was swept in the reverse direction up to -0.3 V vs. Hg|Hg$_2$SO$_4$ at 50 mVs^{-1}.

2.3.3   Galvanostatic electrodeposition on gold macroelectrodes

The electrodeposition of Ni films on Au macroelectrodes was achieve by two seconds constant current pulses. The plating bath composition was 50 mM NiSO$_4 \cdot$6H$_2$O (Sigma Aldrich, 99%) and 0.5 M Na$_2$SO$_4$ (CTR Scientific, 99.9%) with deionized water. The pH of the bath was not adjusted, and had a value between 6 and 7. The applied current was determined using the previously estimated electrode area to get a current density of 4.0 mA cm^{-2}. Potential transients (against the Hg|Hg$_2$SO$_4$ reference electrode) were recorded.

2.3.4   Activation of the Nickel deposits

After the galvanostatic pulse, the success of the electrodeposition was confirmed by cyclic voltammetry in 1 M KOH. The electrode was cycled between -0.4 V and 0.48 V vs. Ag|AgCl and the presence of peaks I$_{af}$ and I$_{cb}$, corresponding to the presence of Ni(OH)$_2$ confirmed that Ni was electrodeposited on the Au surface. Afterwards, the electrode was cycled 30 additional times to promote the formation of a stable NiOOH, which acts as the electrocatalyst for methanol oxidation.
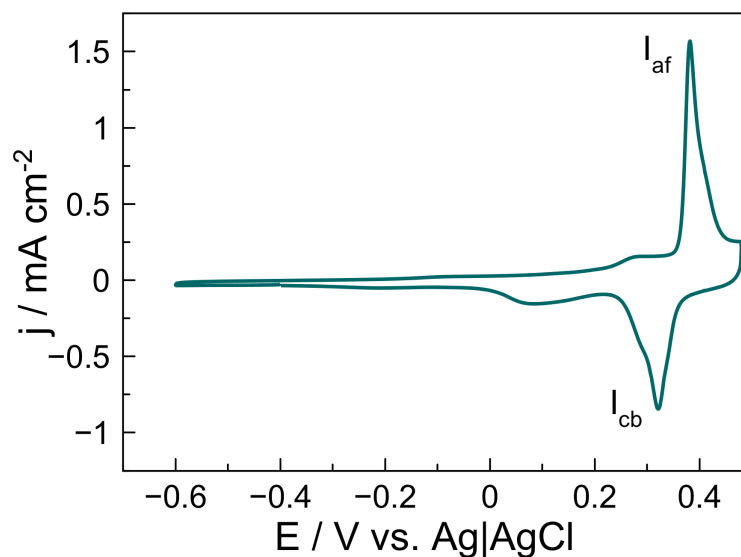
Figure 2.7: Typical cyclic voltammogram of electrodeposited Ni films at 50 mVs^{-1} in 1M KOH.

2.3.5 Methanol oxidation and electrocatalytic activity

For the measurement of catalytic activity, the deposits were tested by cyclic voltammetry in 0.5 M methanol + 1M KOH. The electrodes were polarized from -0.4 to $0.75\,V$ against the reference electrode Ag|AgCl at a sweep rate of $50\,mV\,s^{-1}$ for 30 cycles.

2.4 Sampled Current Voltammetry

Sampled current voltammetry belongs to the family of pulsed voltammetric technique and is produced from the time and current response of a pulsed potential perturbation to a redox system [69, 35]. Voltammograms are built from current transients obtained during constant potential conditions. The current $i(\tau)$ taken at a fixed sampling time τ_s is extracted from all the current transient curves and a sampled current voltammogram is constructed by plotting these currents against the applied potential E.
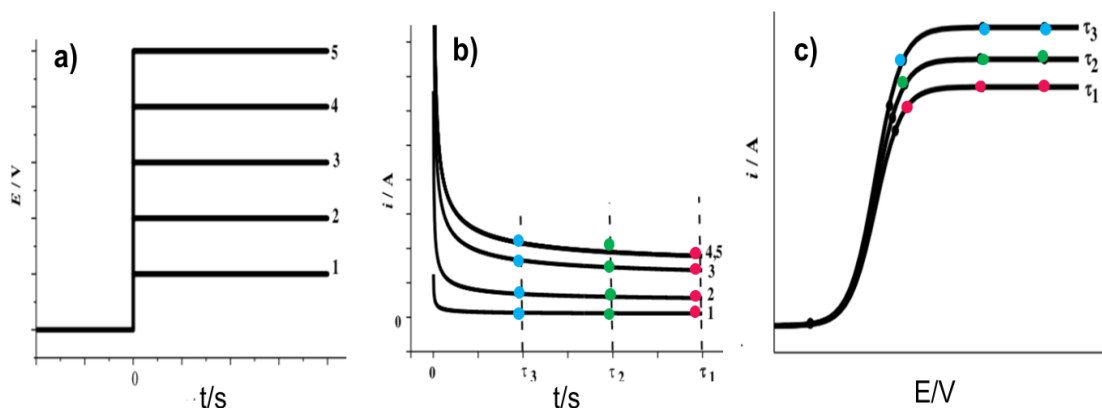
Figure 2.8: Sampled current voltammetry: a) series of potential steps experiments, b) corresponding current transients for potential step experiments, c) reconstructed sampled current voltammograms. Edited from [70].

A script to automate the control of the CH Instruments Model 700D was written both for the electrode pretreatment and collection of sampled current voltammograms.

The electrode potential was always set to initiate at $0.1\,\text{V}$ (vs.Ag|AgCl), where no faradaic processes occur. Then, it was stepped to the potential of interest and held for 3 or $5\,\text{s}$, time during which the chronoamperometric response was recorded. Following this, the potential was changed to -0.1 V and held at this potential for another 3 to $5\,\text{s}$ to guarantee the removal of any nickel oxide present.

A schematic representation of the potential waveform is shown in Figure 2.9. The

same procedure was employed to study the sampled-current voltammetry after Ni activation in $1\,M$ KOH and in $0.5\,M$ methanol corresponding to the electrocatalytic oxidation of methanol.
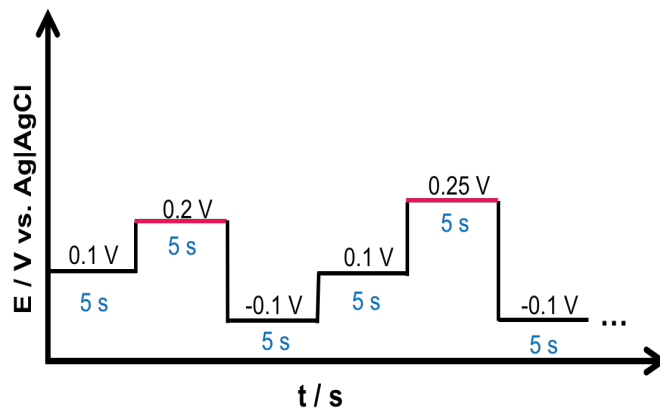
Figure 2.9: Schematic representation of the potential waveform used to the sampled current experiments.

Chapter 3

Results and Discussion

This chapter presents the experimental results and the analysis and interpretation of the electrochemical experiments of nickel electrodeposition, its activation and performance as electrocatalyst in the methanol oxidation reaction. Furthermore, to have a better understanding of the nickel deposition mechanism, self-terminated nickel electrodeposition was studied on microelectrodes and sampled current voltammetry was carried out to extend the understanding of the role of nickel hydroxides and oxyhydroxides in the oxidation of methanol.

3.1   Study of Self-Terminated Electrodeposition

Nickel electrodeposition on Au microelectrodes was studied by cyclic voltammetry using two different reversal potential limits $-1.6\,\mathrm{V}$ and $-1.9\,\mathrm{V}$ vs. MMSE as is shown in Figure 3.1. The nickel plating bath composition was $5.0\,\mathrm{mM}$ $NiSO_4$ + 100 mM Na_2SO_4 with pH=2.69, making Ni^{2+} the dominant species.

The gray dashed curve in Figure 3.1 corresponds to voltammogram obtained in the same supporting electrolyte but in the absence of Ni^{2+}. In this case, HER from

Figure 3.1: Cyclic voltammetry of an Au microelectrode (diameter=50 μm) in 5.0 mM $NiSO_4$ + 100 mM Na_2SO_4 pH 2.69. Dashed line show the supporting electrolyte 100 mM Na_2SO_4 at pH 2.69. Cathodic reversal potentials: blue= -1.6 V, green=-1.9 V.

H_3O^+ reduction reaches its transport-limited current near -1.25 V vs MMSE during the cathodic sweep. Following this, water reduction starts c.a. -1.9 V vs. MMSE.

The presence of Ni^{2+} slows down the raise of the cathodic current, while maintaining the onset almost unchanged. Transport-limited current is reached c.a. -1.5 V vs. MMSE. Around -1.75 V vs. MMSE a sudden current drop is observed, signaling the onset of Ni self-termination by the formation of $Ni(OH)_2$, as described my Moffat et al. [54]. They suggested that this spike was due to autocatalytic H_2 production associated with $Ni(OH)_2$ads nucleation and growth on the Ni surface.

The cathodic current is the sum Ni deposition and HER from H_3O^+ reduction. Thus, the value of the Ni limiting current, $I_L(Ni^{2+})$, can be calculated by subtracting the HER limiting current, measured in the Ni^{2+}-free electrotye, from the total current [54].

Orinakiva et. al proposed that in a sulfate electrolyte Ni electrodeposition follows this mechanism [71, 72]:

$$Ni^{2+} + H_2O \rightarrow NiOH^+ + H^+ \tag{3.1}$$

$$NiOH^+ \rightarrow NiOH^+_{ads} \tag{3.2}$$

$$NiOH^+_{ads} + e^- \rightarrow NiOH_{ads} \tag{3.3}$$

$$NiOH_{ads} + H^+ + e^- \rightarrow Ni + H_2O \tag{3.4}$$

$$2\,H_2O + 2e^- \rightarrow H_2 + 2\,OH^- \tag{3.5}$$
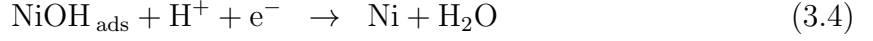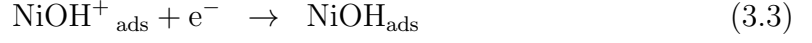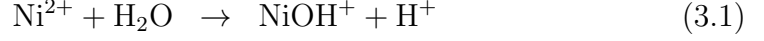
The diffusion coefficients of Ni^{2+} and H_3O^+ were estimated from the limiting currents. The values of D_{Ni} and D_{H^+}, $8.4 \times 10^{-6}\,\mathrm{cm^2\,s^{-1}}$ and $2.1 \times 10^{-4}\,\mathrm{cm^2\,s^{-1}}$ respectively, are in close agreement to those reported in the literature, $5.6 \times 10^{-6}\,\mathrm{cm^2\,s^{-1}}$ for D_{Ni} and $7.9 \times 10^{-5}\,\mathrm{cm^2\,s^{-1}}$ for D_{H^+} [73].

Yu et al. [74] explained that during an electrodeposition process, two limiting processes will be at play: faradaic and diffusion. In the electrodeposition system, if the diffusion rate of species is faster than the reaction rate, the electrodeposition system is controlled by the electrochemical reaction. Otherwise, the electrodeposition is controlled by diffusion.

Figure 3.2 shows that increasing the scan rate has a marginal effect on the cathodic current. On the contrary, the height of the anodic peaks, corresponding to the stripping of Ni, grows significantly as the scan rate increases. The cathodic behavior is what is expected for a diffusion-limited reaction on a microelectrode, while Ni stripping seems to be controlled by electrochemistry reaction. Nickel electrodeposition and self-termination was also studied replacing the sulphate counter-ions by chloride ions as is shown in Figure 3.3

In a chloride rich electrolyte, the dominant precursor is the complexed species $NiCl^+$ and the deposition mechanism commonly accepted is described as follows [71, 75]:
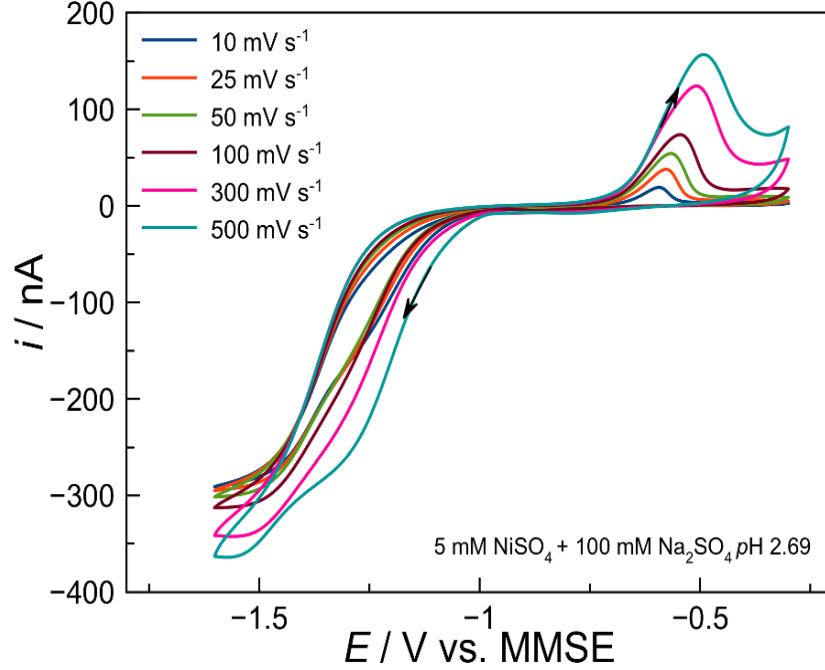
Figure 3.2: Nickel cyclic voltammograms at different scan rates (working electrode: Au 50 μm in diameter) in 5 mM NiSO$_4$ + 100 mM Na$_2$SO$_4$ pH 2.69.

$$\text{Ni}^{2+} + \text{Cl}^- \quad \rightarrow \quad \text{NiCl}^+ \tag{3.6}$$

$$\text{NiCl}^+ \quad \rightarrow \quad \text{NiCl}^+\,\text{ads} \tag{3.7}$$

$$\text{NiCl}^+\,\text{ads} + \text{e}^- \quad \rightarrow \quad \text{NiCl}\,\text{ads} \tag{3.8}$$

$$\text{NiCl}\,\text{ads} + \text{e}^- \quad \rightarrow \quad \text{Ni} + \text{Cl}^- \tag{3.9}$$

$$2\,\text{H}_2\text{O} + 2\text{e}^- \quad \rightarrow \quad \text{H}_2 + 2\,\text{OH}^- \tag{3.10}$$
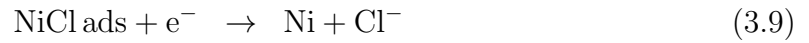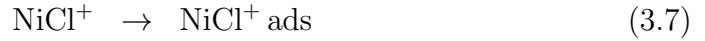
The voltammogram recorded in a Ni^{2+}-free chloride electrolyte shows that the HER onset is cathodically shifted compared to the sulfate bath. This may be due to the adsorption of Cl$^-$ on the gold surface, which blocks the active sites required for HER. Contrary to what is observed in a sulfate bath, in the chloride bath the presence of Ni^{2+} shifts the cathodic current onset to less negative values as nickel electordeposition occurs. In sulfate electrolytes both Ni deposition and HER start at the same time [71].
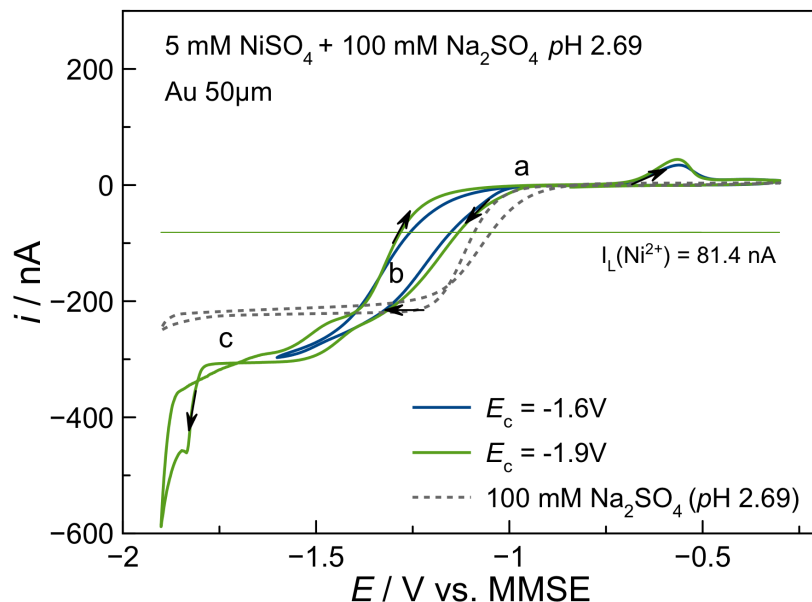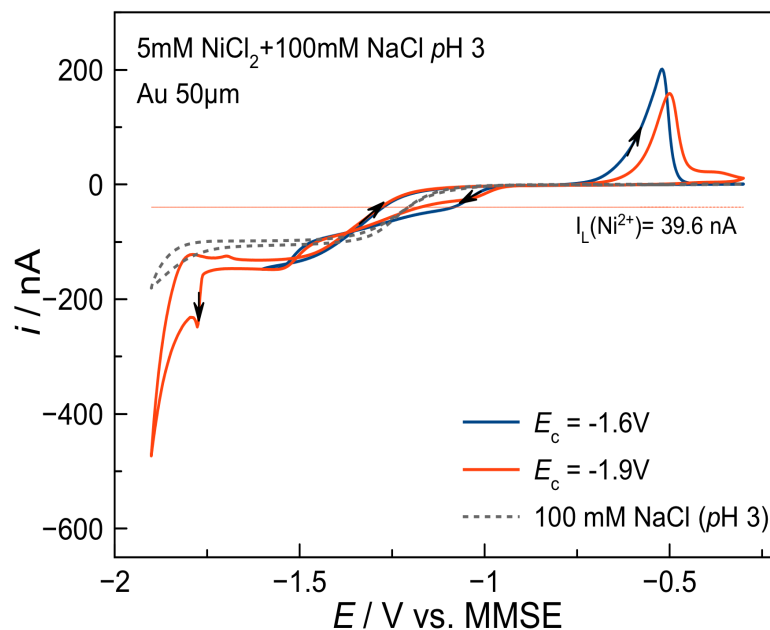
Figure 3.3: Cyclic voltammetry of an Au microelectrode (radius, 25 μm) in 5.0 mM NiCl$_2$ + 100 mM NaCl pH 3. Dashed line is supporting electrolyte 100 mM NaCl at pH 3. Cathodic reversal potentials, of (blue) -1.6 V, (orange) -1.9 V.

As in the sulfates bath, in the chloride bath a spike indicating Ni self-termination is present at around -1.75 V vs. MMSE.

These experiments show that at sufficiently negative potentials, self-termination of Ni electrodeposition will occur. In consequence, the growth of the deposited nickel is constrained by this effect.

3.2 Galvanostatic Electrodeposition

After understanding the effects of pH and supporting electrolyte on Ni electrodeposition and self-termination, galvanostatic electrodeposition was studied on gold macro-electrodes (0.5 mm in diameter). Figure 3.4 shows the typical potential transient of galvanostatic Ni electrodeposition in electrolyte solutions with 50 mM NiSO$_4 \cdot 6$ H$_2$O + 500 mM Na$_2$SO$_4$.
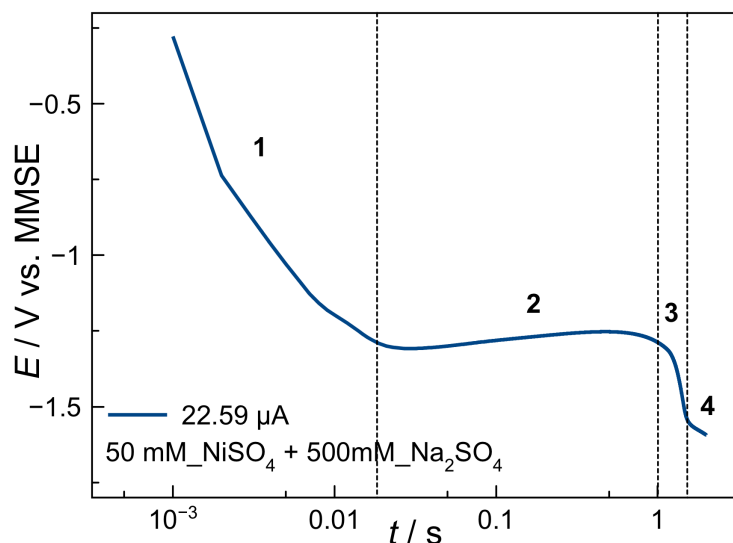
Figure 3.4: Potential transient recorded during a galvanostatic deposition (2 s at 27.59 μA) of Ni from 50 mM NiSO$_4$ $\cdot$ 6 H$_2$O + 500 mM Na$_2$SO$_4$ on a clean Au electrode. A logarithmic time scale was used.

This behavior was reported previously by our group, as was shown in Figure 1.8 and by other works with different substrates. The first regime is related to the nucleation of Ni. The second regime corresponds to the growth of the nuclei the third is associated with the termination of Ni electrodeposition brought by a local change in pH. Finally, the fourth regime can be linked to the reduction of H$_2$O on the nickel deposit.

As mentioned in Chapter 2, Ni thin films were electrodeposited by applying a two-second pulse with an intensity of 4.0 mA cm^{-2}. This current was normalized to the surface area (ECSA) calculated from the Au voltammograms in 0.5 mM H$_2$SO$_4$. The surface areas varied widely between the electrodes, as shown in Figure 2.6 and discussed in section 2.3.3. Consequently, the applied current was significantly different from one experiment to another, but the current density was the same. Figure 3.5 depicts the potential transients of five experiments. The most significant difference between them is the extent of regime 2.

The nuclei growth formed after the initial potential drop should be diffusion limited since no depletion of precursor has yet occurred. Therefore, it should be possible to
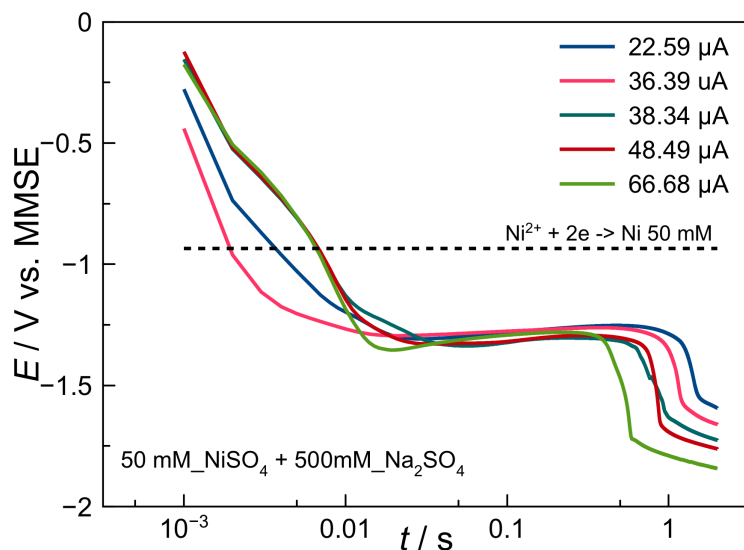
Figure 3.5: Potential transients of five experiments recorded during a galvanostatic deposition of Ni from 50 mM NiSO$_4 \cdot 6$ H$_2$O + 500 mM Na$_2$SO$_4$ on a clean Au electrode. A logarithmic timescale was used.

estimate the duration of regime 2, τ, from Sand's equation 3.11 [7]. Table 3.1 shows that the experimental values of τ are at least one order of magnitude smaller than the theoretical values calculated using the current normalized to the Au surface area. Conversely, a better agreement between the experimental and theoretical values is obtained when the applied current is instead normalized to the geometrical area.

$$\tau^{\frac{1}{2}} = \frac{\pi^{1/2} n F D^{1/2} C^*}{2\,j} \tag{3.11}$$

where j is the current density (i/A).

The area of any electrode can be measured in two different ways. The geometric area, that corresponds to the projected cross-section of the electrode, and the surface area, which takes into account the microscopic features of the electrode. A schematic representation of this is shown in Figure 3.6. The ratio between these two areas is called *roughness factor*.

Table 3.1: Comparison of theoretical and experimental τ for regime 2 of Ni electrodeposition.

Applied Current $\times 10^{-5}$/ A	Theoretical superficial area τ / s	Theoretical geometric area τ / s	Experimental τ / s
3.63	30.18	1.40	1.15
2.26	29.63	3.63	1.40
6.66	29.91	0.42	0.57
4.84	30.05	0.79	0.87
3.83	29.63	1.26	0.93
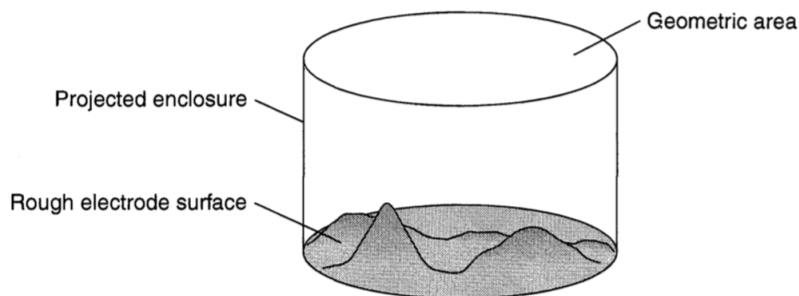
Figure 3.6: Representation of the superficial and geometric area of an electrode. Taken from [35].

The effect of the electrode roughness on the chronopotentiometric response has been previously studied [76]. At short times, the thickness of a diffusion layer is comparable to the microscopic features of the electrode; thus, the diffusion field closely follows the surface area. As the diffusion layer grows, the diffusion field 'sees' the electrode as a flat surface, making the behavior of the electrode dependant on the geometric area [35]. Reinmuth [77] proposed that as the thickness of the diffusion layer decreases and the current density increases, the contribution of the electrode's roughness becomes more prominent, as is represented in Figure 3.7:

Therefore, in chronopotentiometric experiments, the influence of the electrode surface roughness becomes significant for the processes occurring at short time scales.

While regime 2 seems to depend on the geometric area, this may not hold for regime
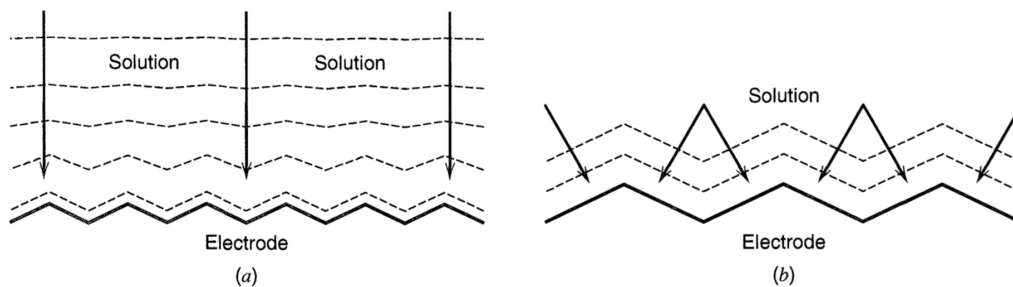
Figure 3.7: Diffusion fields at (a) long and (b) short times. Taken from [35].

1. As mentioned in Chapter 1, the applied current density determines the minimum potential reached during regime 1, and the time it takes to reach. In other words, the more intense the applied current density pulse, the lower it would be. Despite the applied current being so different between experiments, all of them reach more or less the same potential minimum at approximately the same time, as is shown in Table 3.2, suggesting that the nucleation process occurs in a time scale at which the surface area determines the diffusion field.

Table 3.2: Dependence of the potential minimum on the applied current.

Applied current $\times 10^{-5}$ / A	t_{min} / s	E_{min} vs. MMSE / V
2.26	0.027	-1.31
3.63	0.021	-1.29
3.83	0.051	-1.34
4.84	0.031	-1.33
6.66	0.019	-1.35

Additionally, if we compare the theoretical transient times (geometric area) and the experimental transient times, it is evident that the experimental transient time is shorter than the theoretical expected time, except for the two values with the highest current applied. Transition to regime 3 at a shorter time than those fixed by diffusion control hints to self-termination of the electrodeposition process.

3.3 Activation of the nickel electrocatalyst

When immersed in an alkaline solution, the nickel deposit surface is immediately covered by a layer of nickel hydroxide [28, 78]. The following scheme describes the mechanism of nickel oxidation in alkaline media proposed by Bode et al. [79]:
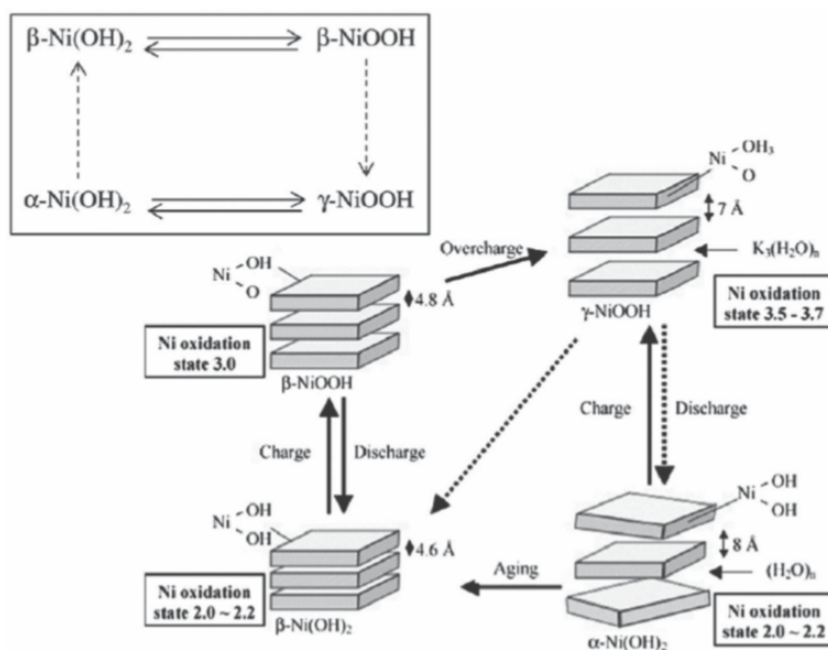
Figure 3.8: Bode's diagram. The interlayer distances and average Ni oxidation states are shown for the four phases. Taken from [80].

According to this scheme, Ni can form different phases in alkaline media by oxidation of Ni(II) into Ni(III). Trafela et al. [81] studied the Ni redox couple on nickel nanowires (Figure 3.9). The fist reaction is the nickel oxidation $Ni + 2OH^- \rightleftharpoons \alpha\text{-Ni(OH)}_2 + 2e^-$, which manifests as an anodic current peak (a1) around $-0.15\,\text{V}$ vs. Ag|AgCl. At more positive potentials, the $\alpha\text{-Ni(OH)}_2$ is converted to the $\beta\text{-Ni(OH)}_2$ form (a2). Due to its high electrochemical stability, $\beta\text{-Ni(OH)}_2$ [79, 82] cannot be electrochemically reduced or removed from the surface of the electrode. Taking the potential to more positive values, the next peak (a3) is observed at a potential of 0.5 V vs. Ag|AgCl; this peak is related to the Ni oxidation from Ni(II) to Ni(III), where $\beta\text{-Ni(OH)}_2$ is

oxidized to β-NiOOH. In the reverse sweep, the cathodic peak at $0.4\,\text{V}$ (c1), represents the reduction of β-NiOOH to β-Ni(OH)$_2$. These results show the progressive transformation of Ni(II) to Ni(III) due to the insertion of OH$^-$ into the Ni(OH)$_2$ and NiO layers.
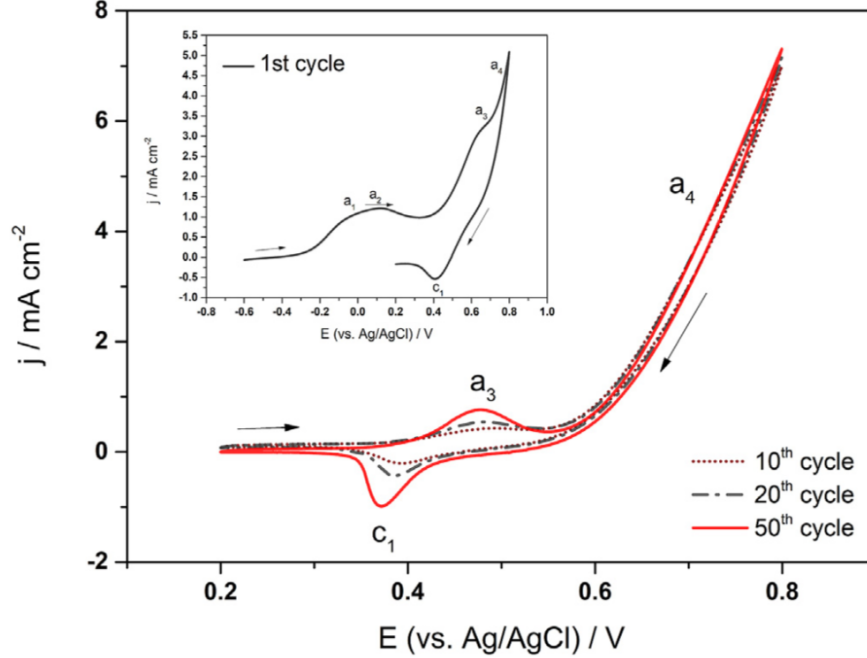
Figure 3.9: Cyclic voltammogram of Ni-NW-based electrode in $0.5\,\text{M}$ KOH at a scan rate of $200\,\text{mVs}^{-1}$: 10th cycle (dotted curve), 20th cycle (dashed curve), 50th cycle (red solid curve). Taken from [81].

After the galvanostatic electrodeposition step, the working electrode was subjected to a single cyclic voltammetry scan in 1 M KOH from -0.4 to $0.48\,\text{V}$ vs. Ag|AgCl, to confirm the presence of nickel on its surface. In Figure 3.10, two peaks similar to those in Figure 3.9 can be observed, and correspond to reaction 3.12 [83, 84]. These processes prove that the nickel electrodeposition was achieved successfully.

$$Ni(OH)_2 + OH^- \rightleftharpoons NiOOH + H_2O + e^- \qquad (3.12)$$
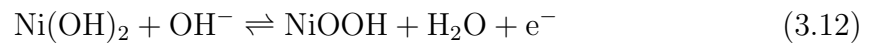
The electrodes were continuously cycled until a steady-state was reached, which is

attained after 30 cycles. Depending on the initial state of the surface of the nickel, this activation could have a small or large effect on the shape, height, and position of the anodic and cathodic peaks. This is associated to different ratios of α- and β-Ni(OH)$_2$ present in the activated deposit [85, 86, 81].
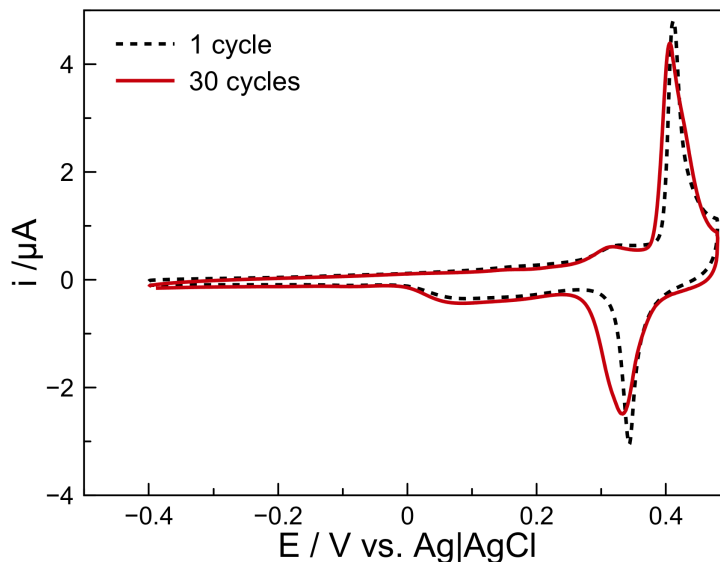
Figure 3.10: Cyclic voltammogram of electrodeposited Ni films on Au electrodes and Ni electrodes at 50 mV s^{-1} in 1M KOH.

A similar activation process was also carried out on nickel wire electrodes (diameter 5 mm) for comparison purposes. Figure 3.11 shows the activation voltammograms of the nickel deposits generated by galvanostatic deposition (see Fig.3.5) and the nickel wire electrodes. The voltammograms overlap almost perfectly in the range from -0.5 to 0.3 V vs. Ag|AgCl. The main difference between them in the location Ni(OH)$_2$ peak. According Kostecki, Yeo, and Barned [87, 85] the oxidation of α-Ni(OH)$_2$, takes places at 0.343 ± 0.002 V vs.Ag|AglCl, while β-Ni(OH)$_2$ occurs at 0.398 ± 0.007 V vs.Ag|AglCl. Despite the fact that reversible potentials of the α/γ and β/β couples are difficult to determine, there is general agreement that α-Ni(OH)$_2$ is oxidized to γ-NiOOH at a lower potential than the corresponding oxidation of β-Ni(OH)$_2$ to β-NiOOH.

The Ni electrodeposits can be separated in two groups, based on the position of the

NiOOH peak. This is supported by the fact that the deposits generated using currents in the range of 22–33 μA present the a peak corresponding to the formation of NiOOH appears below 0.39 V vs. Ag|AgCl. These materials will be referred to as Group A (long-dashed curves in Fig. 3.11), while the ones produced by pulses between 38 and 66 μA present this process above 0.39 V vs. Ag|AgCl and will be classified in Group B (short-dashed curves in Fig. 3.11). This suggests that there is an applied current threshold separating group A and group B behaviors. The assignment of Ni deposits as Group A or Group B Ni helps to emphasize the different content of β-NiOOH and γ-NiOOH present in these materials. Nevertheless, other factors such as morphology may play a role on the shift on the peak potential. Since the nucleation of the Ni deposits appears to be similar for all these electrodes, this difference must be rather caused by the growth process.
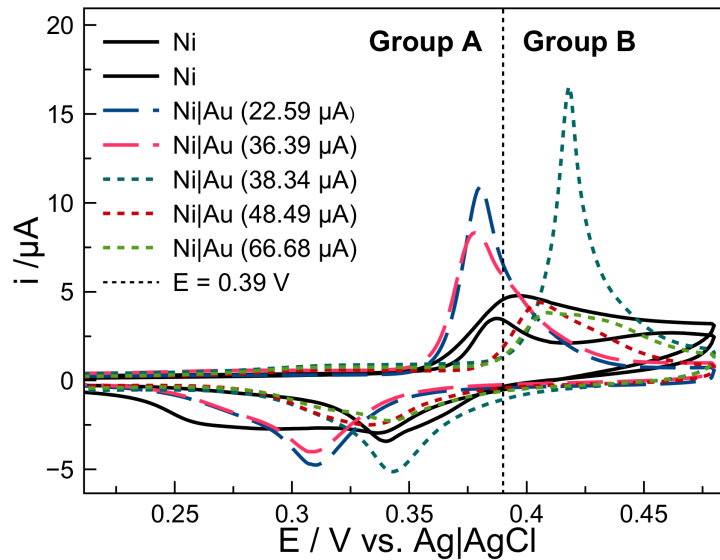
Figure 3.11: Cyclic voltammogram of Ni wire electrodes (solid curves), Group A (long-dashed curves), and Group B Ni films (short-dashed curves). Scan rate: 50 mV s^{-1}, electrolyte: 1M KOH.

NiOOH surface concentration Γ was estimated using the following equation [88]:

$$\Gamma = \frac{Q}{nFA} \tag{3.13}$$

50

where Q is the charge transferred in the of the activation process, area under the peak I_{af}, F is the Faraday constant, n is the number of electrons transferred in the redox process between $Ni(OH)_2$ and $NiOOH$ (3.13), i.e. 1, and A is the geometric area of the electrode ($1.964 \times 10^{-3}\,cm^2$). Most mechanisms for methanol electrooxidation agree in that NiOOH plays the role of the electrocatalyst, thus the number of available active sites for this reaction is proportional to Γ.
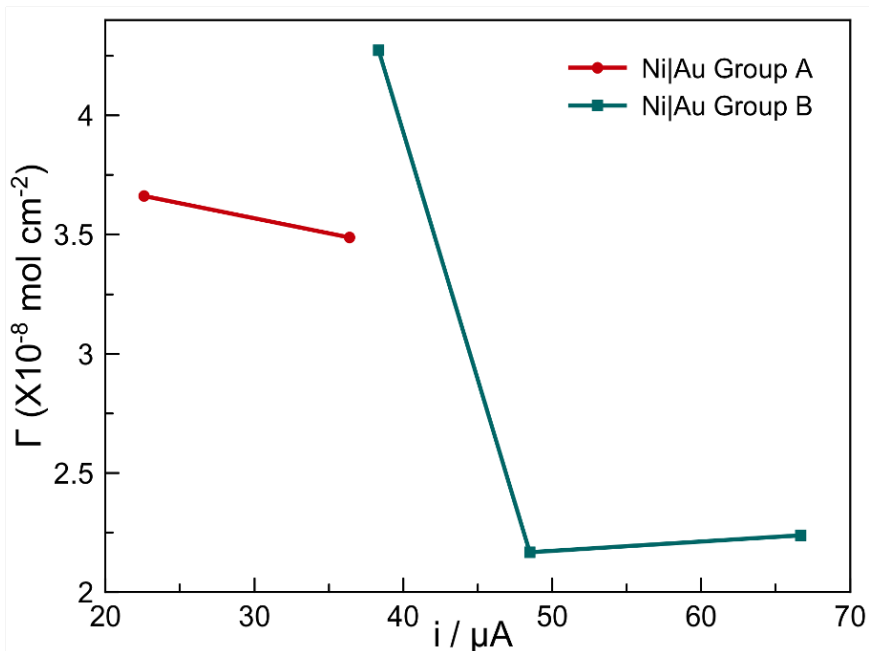
Figure 3.12: Dependence of the surface concentration of NiOOH (Γ) on the current pulse applied in the presence of ions SO_4^{2-}.

Figure 3.12 shows the dependence of Γ with the applied electrodeposition current. The highest Γ value ($4.27 \times 10^{-8}\,mol\,cm^{-2}$) for nickel electrodeposits was obtained in the deposition with a 38.34 μA. This is the only electrode from Group B Ni films with a high Γ, the other have a Γ value of almost half of group A's Γ. This brings back the importance of the growth stage of the electrodeposition and hints that there is a threshold close to the 38.34 μA pulse that separates both Groups.

3.4 Methanol Electrooxidation

The electrocatalytic activity of nickel deposits was evaluated by clyclic voltametry in 1 M KOH + 0.5 M methanol. A typical methanol electro-oxidation voltammogram for Ni electrodeposited on Au is shown in Figure 3.13. In this voltammogram, a pair of peaks are observed, I_{af} and I_{cb}, at potentials around 0.34 and 0.29 V vs. Ag|AgCl corresponding to the Ni(II) / Ni (III) redox pair.

In agreement with the experiments reported by Taraszewska *et al.* [89], methanol oxidation on the Ni deposits begins after the formation of the NiOOH species. This process corresponds to peak II_{af} and arises from the oxidation of methanol and adsorbed intermediates. After reversing the potential, poisoning intermediates are desorbed, freeing NiOOH active sites, which results in a second anodic peak, II_{ab}. On $Ni(OH)_2$, the main product of methanol oxidation is formate ion; thus it is a four-electron reaction [89, 90, 91]:

$$CH_3OH + 5\,OH^- \rightarrow HCOO^- + 4\,H_2O + 4\,e^- \tag{3.14}$$
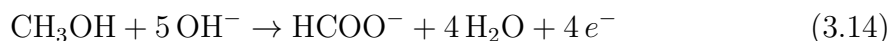
Methanol oxidation was studied on gold electrodes modified by the deposited nickel thin-films, and on a nickel electrode, their corresponding voltammograms are shown in Figure 3.13. The inset in this figure shows the characteristic peaks related to the oxidation of $Ni(OH)_2$ to NiOOH. The pink curve corresponds to a Group A Ni deposit, generated with an applied current was 36.39 μA, while the green curve belongs to a Group B Ni film, produced at 38.31 μA. For the nickel wire electrode, the anodic peak corresponding to the NiOOH formation was narrower, and its potential is located between those of Group A and Group B.

The electrocatalytic intensity (EI), defined by Ding [43] as the sum of the currents of the peaks II_{af} and II_{ab}, was calculated to estimate the electrocatalytic performance of the nickel deposits. These values are tabulated in table 3.3. It becomes evident that
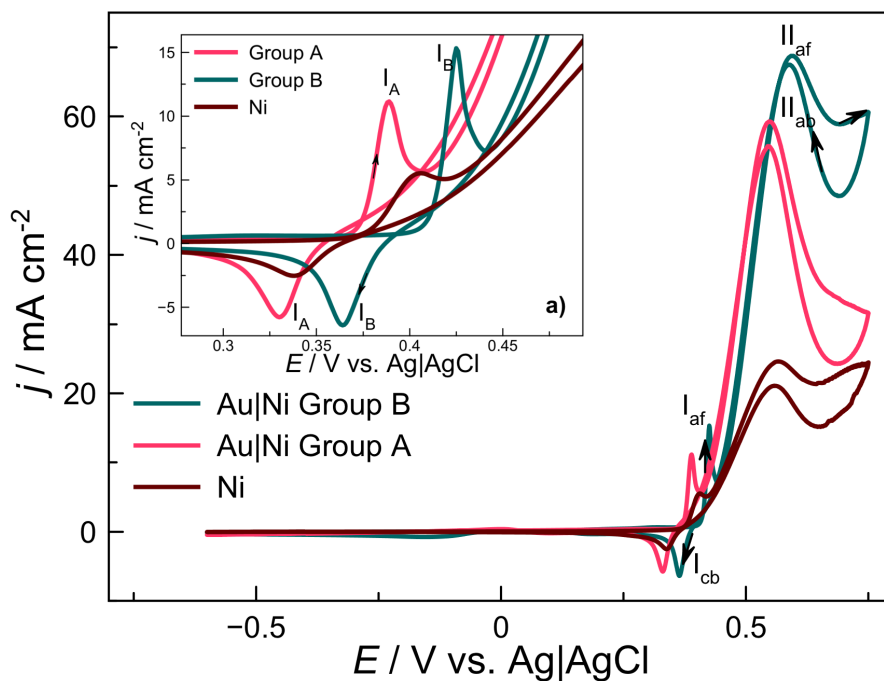
Figure 3.13: Cyclic voltammetry of methanol oxidation on activated Ni and group A and group B Ni deposited on gold. The electrolyte is $1\,M\,KOH + 0.5\,M\,CH_3OH$ at a sweep rate of $50\,mV\,s^{-1}$. The scan was recorded after 30 cycles of stabilization.

the lowest electrocatalytic activity was obtained with nickel wire electrodes. Rahim [65] reported that bulk nickel electrodes are not a good catalyst for methanol oxidation due to the formation of dense layers that render a poor conductivity, difficulting the electron transfer through the film itself. Additionally, Tarazewska et al. [89] reported that the formation of a dense oxide layer decreases the number of the active sites available for methanol oxidation reaction reducing its electrocatalytic activity. On the other hand, nickel films from groups A and B have similar values of Γ but it is

Table 3.3: Dependence of the current applied and Γ on the EI

Electrode	Applied current/ $10^{-5}\,\mathbf{A}$	Γ / $10^{-8}\,cm^{-2}$	EI / $mA\,cm^{-2}$ ˆ
Au|Ni (A)	3.63	3.03	115
Au|Ni (B)	3.83	3.42	136
Ni	NA	1.42	46

the latter that shows higher EI, associated to a higher β-Ni(OH)$_2$ content. Previous works by Chen and Guo [56, 92, 90] reported that β-NiOOH is identified as the most active material for methanol oxidation, because it high stability in strong alkaline electrolytes.

3.5 Sampled Current Voltammetry

As mentioned in section 2.4, sampled current voltammograms are constructed by sampling a series of current transients at a fixed time (τ_s). The sampling time τ_s may be used to derive an equivalence to the scan rate, ν or a sweep voltammetry, given by [35]:

$$\tau_s = \frac{RT}{F\nu} \tag{3.15}$$

where T is the temperature, R gas constant, F Faraday constant and ν scan rate.

In a linear sweep mode, the gradual increase in the potential implies that the current in a subsequent step depends on the previous measurement [69]. In the sampled current voltammetry, the measurement for each potential step is referred to an initial potential, E_i, at which the no faradaic process occurs, and thus the base current is zero. Therefore, the current is determined by the potential step itself.

The present study was undertaken to study the nickel hydroxide oxidation and oxidation of methanol with electrodes treated in such a way that every point on the current-voltage curve had the same electrode history.

3.5.1 Sampled Current Voltammetry in 1 M KOH

Sampled Current Voltammetry was studied after the nickel electrodeposits were activated in alkaline media. The potential waveform (Figure 2.9) was designed to refresh the electrode surface before each potential step, ensuring that every point on the

sampled-current voltammogram corresponds to an equivalent state and the whole waveform is repeated keeping all parameters the same, except the potential of the final step. The experimental procedure is described in section 2.4. Figure 3.14a shows activation voltammogram of a Ni wire electrode at 50 mV s^{-1} with its equivalent sampled-current voltammogram. There is a good agreement between both voltammograms in the 0.2 and 0.37 V vs. Ag|AgCl range. Both curves exhibit an anodic wave corresponding to the NiOOH formation, although for the sampled voltammogram this wave has lower current and is shifted towards more positive potential values.
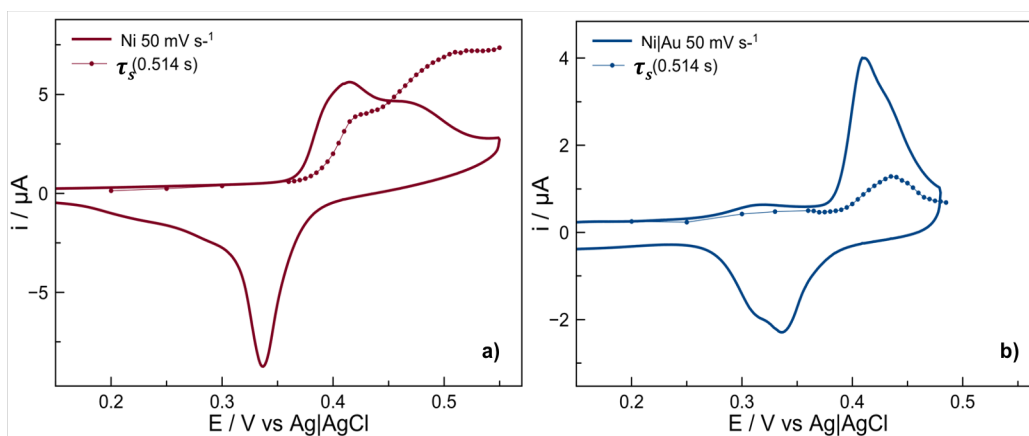
Figure 3.14: Cyclic voltammograms of a) a Ni wire electrode b) Ni films on gold electrode at 50 mVs^{-1} with their respective sampled-current voltammogram in 1M KOH.

A similar behavior can be observed for the Ni electrodeposits as is shown in Figure 3.14b. The NiOOH peak of the sampled current voltammogram is significantly smaller and is anodically shifted, compared to its cyclic voltammetry equivalent. Upon closer inspection, the cyclic voltammetry peak seems to be the merging of two peaks. This suggests a mixed composition of α and β-Ni(OH)$_2$ [87, 93]. Conversely, the peak of the sampled voltammogram does not exhibit any shoulders or hints of merged peaks, suggesting the presence of only one of those two phases. Since the β-NiOOH has the highest formation potential [85, 86, 82] it appears that this is the phase present in sampled current voltammetry. Oliva et al. [82] pointed out that while γ-NiOOH is the

most stable oxidation product, thermodynamically speaking, β-NiOOH would form first. This is because the formation γ-NiOOH entails the the intercalation of water molecules and sheet glide,which adds a of kinetic and steric hindrance to the process compared to β-NiOOH that only need the removal of one proton and one electron. In cyclic voltammetry, slow enough scan rates, the electrode has enough time to form the γ-NiOOH. In contrast, the sampled current voltammogram is constructed from a series of potential pulses. Each pulse takes the electrode from the same initial potential to the target potential in an immediate manner, allowing no time for the formation of γ-NiOOH. At potentials higher than 0.45 V vs Ag|AgCl, the nickel electrode shows a second current wave that is absent on the Ni on gold.

Sampled current voltammograms for the activation process were constructed selecting different sampling times (equivalent scan rates from 10 to 500 mV/s) as shown in the cascade plots of Figure 3.15. For all the sampled current voltammograms, for both wire and electrodeposited nickel electrodes, a peak corresponding to NiOOH formation is present at potentials larger than 0.4 V vs. Ag|AgCl. As τ_s becomes smaller, i.e. faster equivalent scan rates, the peak's height increases. The second wave of the Ni wire electrode becomes masked by oxygen evolution reaction (OER) at τ_s values smaller than 0.343 s, i.e. equivalent scan rates faster than 75 mV s^{-1}. For comparison, oxygen evolution on the electrodeposited Ni electrode is observed only at sampling times shorter than 70 ms (equivalent scan rates faster than 350 mV s^{-1}). It is noteworthy that for the Ni wire electrode, the NiOOH peak and the oxygen evolution onset remain separate, while for the electrodeposited Ni these merge. From which it can be concluded that under the experimental conditions of the sampled voltammetry experiments, the formation of β-NiOOH is favored. This is supported by the shape and position of the redox peak, and the increased oxygen evolution currents. The catalytic activity for OER can be evaluated by the distance between the NiOOH peak and the onset of OER [94]. Under this criterion, the electrodeposited Ni seems to have higher electrocatalytic activity, since the OER onset and NiOOH peak merge. However, as time progresses its activity is significantly diminished, making
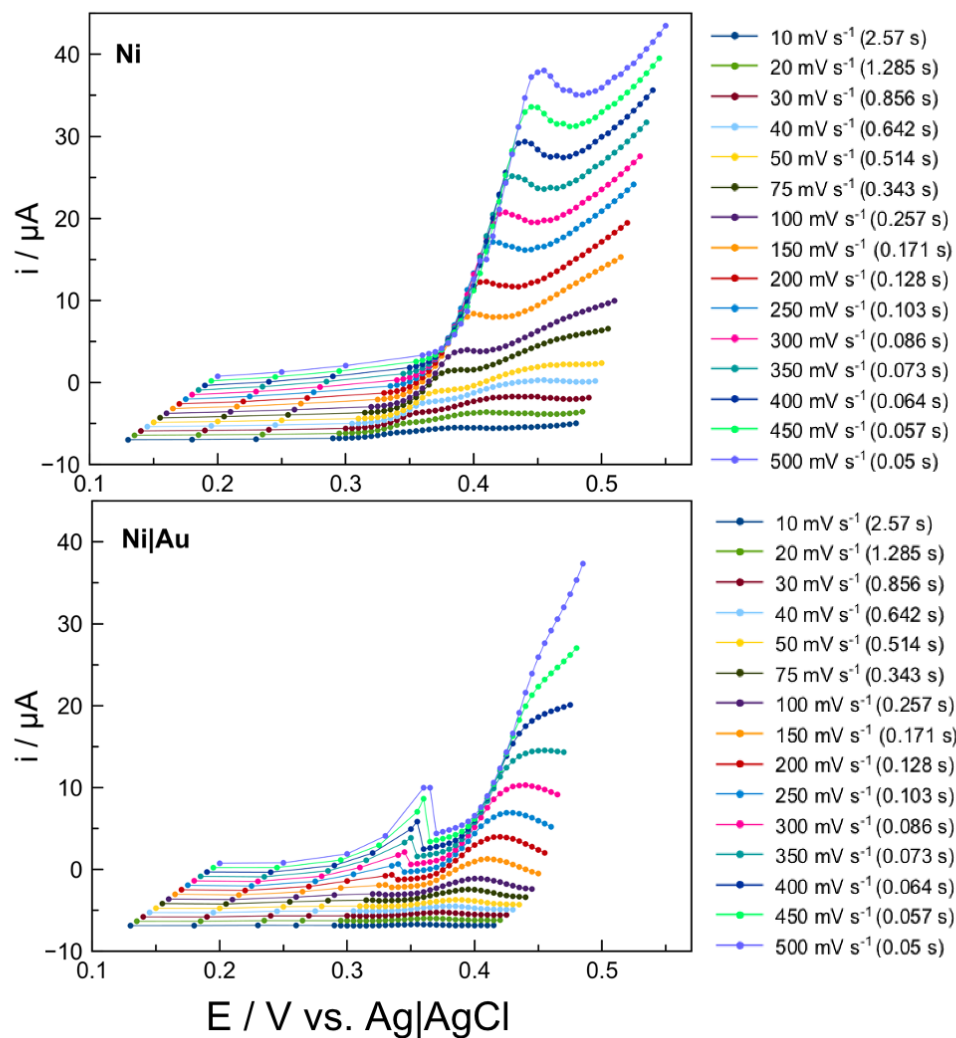
Figure 3.15: Sampled-current voltammograms of Ni films on Au electrodes at different equivalent scan rates in 1M KOH.

OER undetectable at τ_s times larger than 73 ms, while the macroscopic Ni electrode retains its activity for sampling times longer than 300 ms.

3.5.2 Sampled Current Voltammetry in 1 M KOH + 0.5 M Methanol

Figure 3.16 shows a cyclic voltammogram of a Ni wire electrode at $50\ \mathrm{mV\,s^{-1}}$ with their respective sampled-current voltammogram in 1M KOH + 0.5 M methanol. The small anodic peak corresponding to the β-NiOOH formation, present in Figure 3.14 is absent here. Up to 0.6 V vs. Ag|AgCl the sampled-current voltammogram follows the characteristic shape of methanol oxidation at more positive potentials, with the only difference that it reaches higher currents. We can infer that in the SCV experiment, β-NiOOH acts as the electrocatalyst [65]. In section 3.3, we discussed that β-NiOOH is the best electrocatalyst for methanol oxidation. Since γ-NiOOH contains water molecules intercalated between its layers, producing volume expansion or swelling of nickel film and the formation of microcracks and disintegration of the nickel films [92]. Therefore, best efficiency is achieved with β-NiOOH deposits because it has lower intra-layer spacing that results in lower internal resistance [95, 96]. Above 0.6 V vs. Ag|AgCl the sampled current signal becomes noisy, most likely due to oxygen bubbles formed on the electrode.

Sampled current voltammetry on nickel electrode was studied at different equivalent scan rates, as is shown in Figure 3.17. In all the sampled-current voltammograms the characteristic shape corresponding of methanol oxidation appears while the peak corresponding to the formation of NiOOH is absent.

Sampled current voltammetry was used to compare methanol oxidation reaction on Group A and Group B Ni deposits. Figures 3.18a and 3.18b show that the NiOOH peak is absent in both types of Ni films when the sampling time is 0.514 s (equivalent to $50\ \mathrm{mV\,s^{-1}}$. This peak is present at faster equivalent scan rates (Figure3.18c and 3.18d), but its height is significantly smaller than what is observed in their cyclic voltammetry counterparts. This behavior is similar to the one observed in 1 M KOH, hinting that for electrodeposited Ni films sample current voltammetry also favored
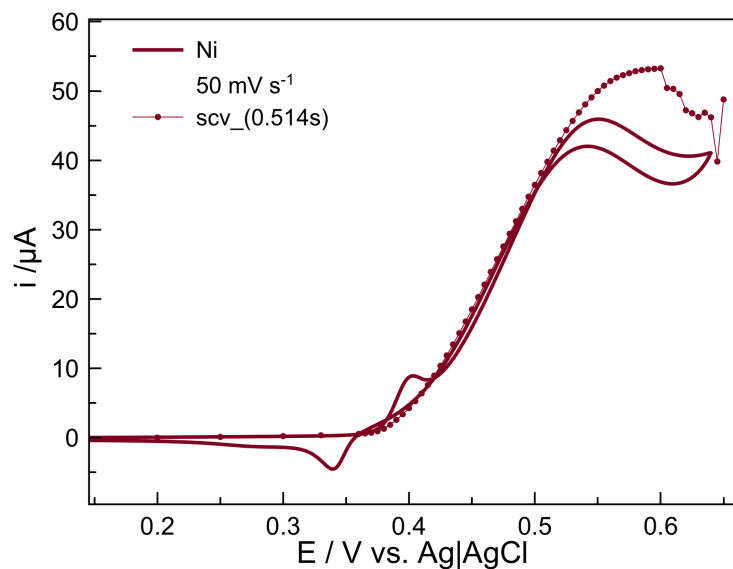
Figure 3.16: Cyclic voltammogram of Ni wire electrode at 50 mVs^{-1} with their respective sampled-current voltammogram in 1M KOH + 0.5 M methanol.
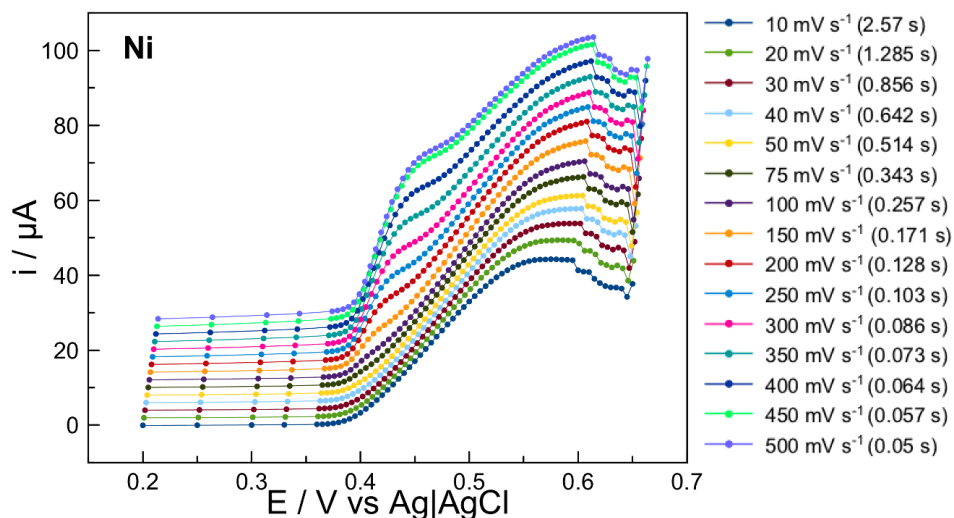
Figure 3.17: Sampled-current voltammogram of a Ni wire electrode at different equivalent scan rates in 1 M KOH + 0.5 M methanol.

the formation of β-NiOOH. The current for methanol oxidation of the Group A film is smaller than the one observed by cyclic voltammetry at both sampling times, but their shapes are quite similar. For Group B electrodes, in contrast, exhibit larger currents and are qualitatively different, suggesting the presence of OER at potentials above 0.55 V vs. Ag|AgCl. Furthermore, The onset for methanol oxidation in Group

A electrodes is located at lower potentials, which indicates higher electrocatalytic activity.
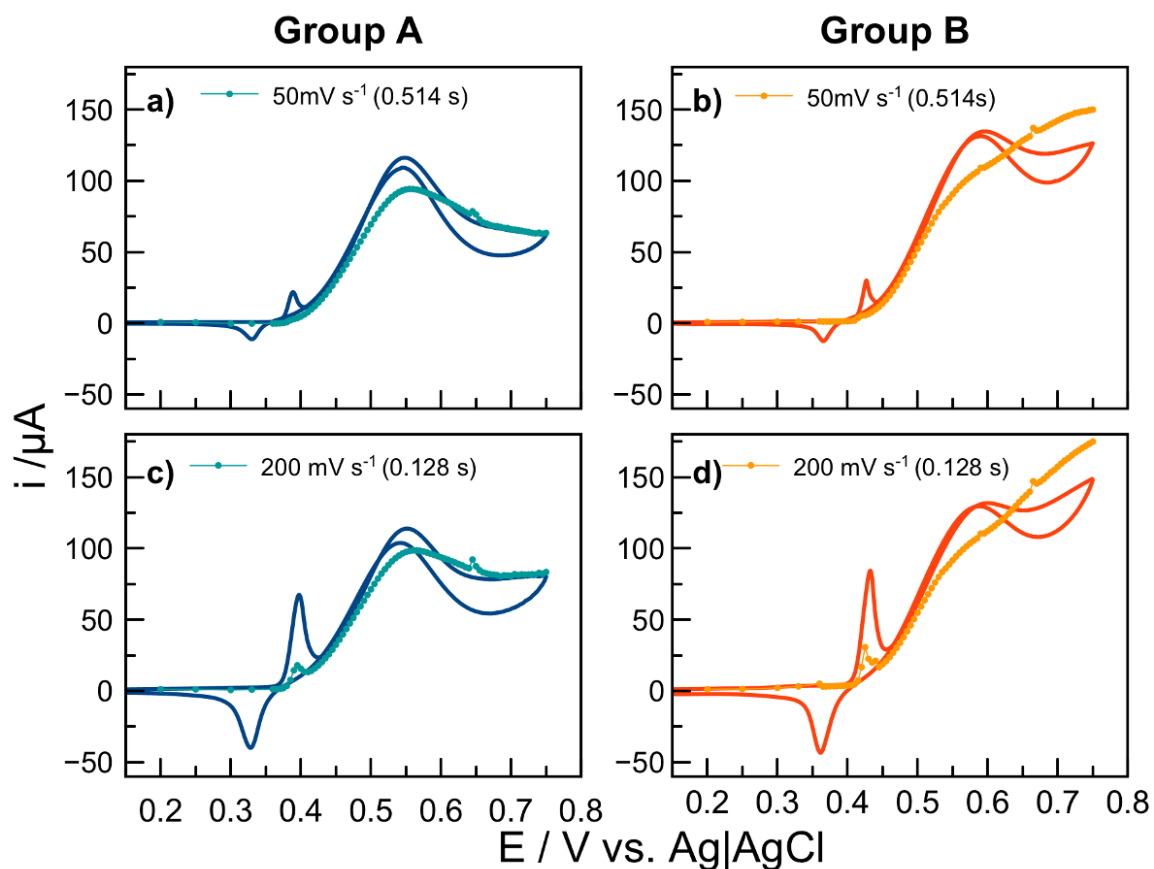
Figure 3.18: Sampled-current voltammogram of Group A and Group B Ni films on gold electrodes in 1M KOH + 0.5 M methanol. At different equivalent scan rates.

Figure 3.19 shows the cascade plots of sampled current voltammetries of Group A and Group B deposits at different sampling times in 1M KOH + 0.5 M methanol. In both cases it is evident that the NiOOH peak can only be seen at equivalent scan rates faster than 75 mV s^{-1}. The height of this peak increases noticeable at shorter sampling times; conversely, the magnitude and shape of the methanol oxidation waves do not change so drastically. While the Group B electrodes exhibit larger oxidation currents, these seem to present OER activity at all sampling times. On the other hand, Group A electrodes exhibit a clear methanol oxidation peak, free of OER interference.
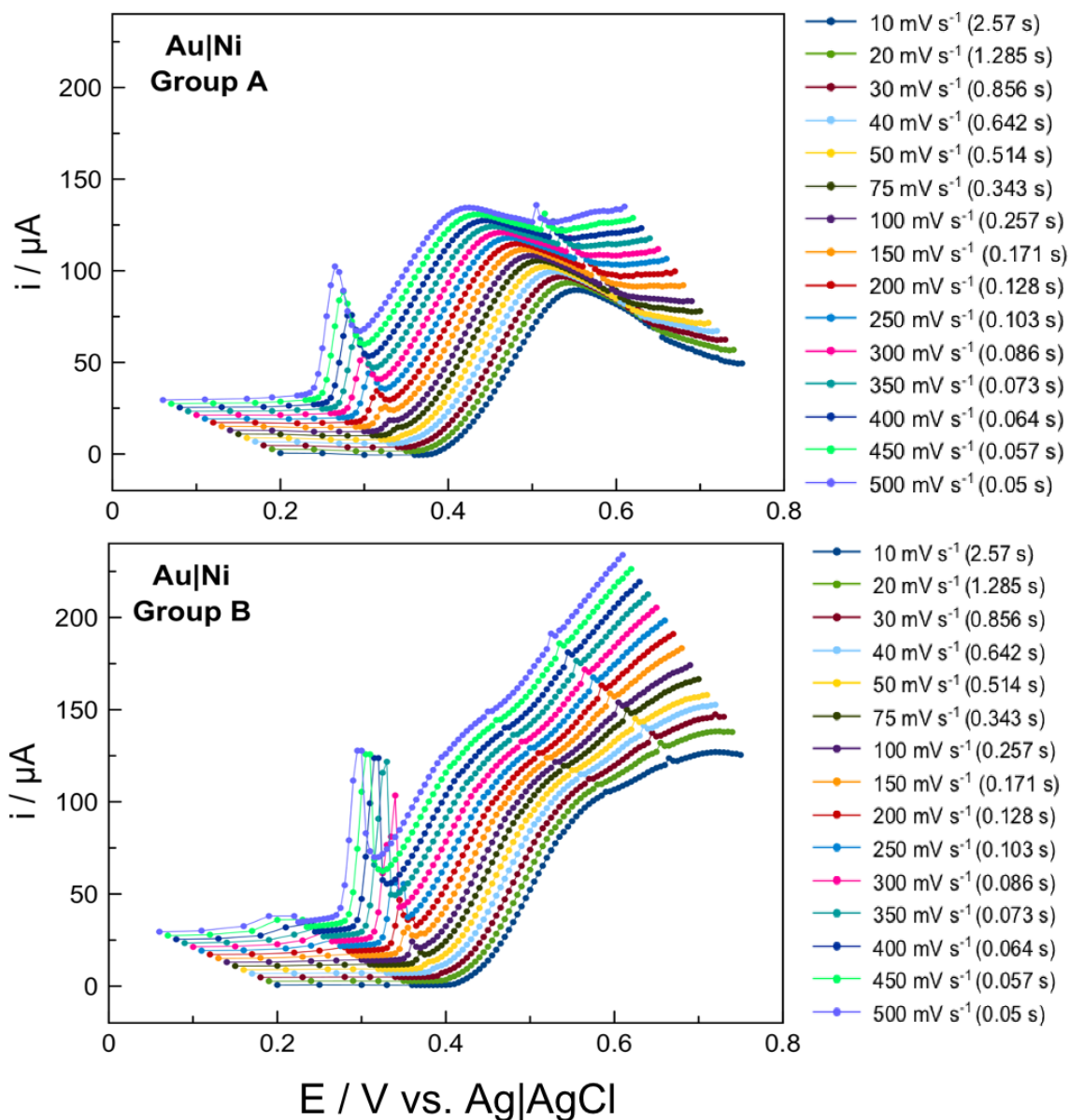
Figure 3.19: Sampled-current voltammograms of Ni films on gold electrodes related with a) Group A and b) Group B at different equivalent scan rates in 1M KOH + 0.5 M methanol.

Lyons et al [97] reported that the oxidation product of β-Ni(OH)$_2$ is the optimum type of oxide for the catalysis of the OER. Additionally, Chen [56] concluded that nickel is more suitable to be used as a catalyst for oxygen evolution rather than methanol oxidation. The experimental results of this work suggest that two types of Ni films can be obtained by galvanostatic deposition. Group A which is a good

catalyst for methanol oxidation, due to its low onset potential and it shows no signs of OER interference. Group B on the other hand, shows catalytic activity for methanol oxidation, but it is a electrocatalyst for OER. Since the nucleation conditions for both types of Ni films were the same, i.e. same surface normalized current density, this shows the importance of the growth stage on the catalytic activity of the final material.

The results presented in Figures 3.19 and 3.17 clearly demonstrate that Ni hydroxide formed on the electrodeposited Ni has a significantly higher OER and MOR activity relative to a thick layer of Ni hydroxide formed on bulk Ni. Yang et al.[98] measured the activity of bimetallic AuNi films for the electrochemical oxidation of methanol and observed that the highest activity occurs for a bulk Au/Ni ratio of 85:15. Furthermore, we can infer the high activity of Ni oxide on Au is due to the charge transfer from the oxide to the highly electronegative Au, leading to the possible formation of a mixed Ni/Au surface oxide than the nickel. The catalytic activity of a given Ni electrode is dependent not only on the amount of redox active material but also on the nature of that material [85].

Chapter 4

Conclusions

Nickel self-terminated electrodeposition was studied on gold microelectrodes by cyclic voltammetry. The well-defined mass transport conditions associated with the microelectrodes provided several insights into the electrodeposition of Ni on Au in $NiSO_4 - Na_2SO_4$ and $NiCl_2 - NaCl$ electrolytes. The voltammograms in both electrolytes revealed a sharp current spike that was correlated with the self-termination of Ni electrodeposition and the onset of the H_2O reduction. These observations were similar to the reported by Moffat [54] where they suggested that this spike was due to autocatalytic H_2 production associated with $Ni(OH)_2$ads nucleation and growth on the Ni surface. These experiments show that at sufficiently negative potential self-termination of Ni electrodeposition will occur, limiting the dimensions of the deposited Ni.

Nickel films were successfully electrodeposited on gold substrates through the use of the galvanostatic method. The role of the Au electrode roughness on the galvanostatic deposition process could be studied. Applying pulses with the same current density normalized to the Au surface area led to similar behaviors during regime 1, the minimal potential was reached more or less at the same potential value and at approximately the same time, suggesting that the nucleation process occurs in a

time scale at which the surface area determines the diffusion field. The different time length of region 2 for each electrode implies that the geometric area is the one defining the diffusion field during the nuclei's growth. Therefore, we can conclude that the geometric and the superficial areas play meaningful roles at different stages, due to the different time scales of the nucleation and growth processes. The self-termination of Ni electrodeposition was evidenced by the discrepancy between the theoretical and experimental τ values.

Cyclic voltammetry in 1 M KOH of the electrodeposited Ni films showed that the applied deposition current had an important effect on the NiOOH peak position. Nickel films deposited at applied currents in the range of 22–33 μA had this peak below 0.39 V vs. Ag|AgCl, they were classified as Group A deposits. Group B comprised films deposited by pulses in the range of 38 μA to 66 μA, they NiOOH peak for these electrodes appeared above 0.39 V vs. Ag|AgCl. These difference in behavior is most likely caused by different content of β-NiOOH and γ-NiOOH and different morphologies. The correlation between applied current and NiOOH peak position suggests a threshold value separating group A and group B behaviors. Since the nucleation stage was almost identical, as evidenced by the same $E_{\min}$ and $t_{\min}$ values, the different behavior must be a consequence of the different conditions of the growth stage.

The electrocatalytic activity of nickel deposits was evaluated by cyclic voltammetry in 1 M KOH + 0.5 M methanol. The lowest electrocatalytic activity was obtained with nickel wire electrode, confirming what was previously reported in the literature [92]. In contrast, nickel films of groups A and B have similar values of NiOOH surface concentration; however, the latter shows higher catalytic activity with a value of 136.2 mA cm^{-2}. Under similar conditions, the EI intensity of the best catalyst reported by our group, which was 90 mA cm^{-2}. Considering that the applied current density, normalized to the geometric area, this suggests that Ni films' catalytic activity can

be enhanced by tuning the growth stage.

Sampled current voltammetry technique was employed to complement the study of the activation of the nickel surface and its methanol oxidation mechanism. The NiOOH peak in the sampled current voltammograms showed some differences in shape and size, compared to the cyclic voltammograms. These differences were assigned to the higher β-NiOOH character of the sample current voltammetry measurements. This is to be expected because, for sample current voltammetry, each pulse takes the electrode from the same initial potential to the target potential in a prompt manner, without enough time for the formation of γ-NiOOH. The experimental results of this work suggest that two types of Ni films can be obtained by galvanostatic deposition. Group A deposits are good electrocatalyst for methanol oxidation due to their low onset potential and no signs of OER interference. Group B, on the other hand, shows electrocatalytic activity for methanol oxidation, but it is a better catalyst for OER.

Future work

The results presented in this work and discussions can be taken as a starting point for future work.

The substrate roughness is a characteristic that influences the deposition mechanism, so a correlation of particle size and pulsed current has to be achieved by the use of characterization techniques such as scanning electron microscopy (SEM), atomic force microscopy (AFM). The double current pulse is recommended to study the nickel electrodeposition to understand better the control of the nucleation and growth of the nickel nuclei and compare it with the deposits obtained in this work. In this work, there were made some assumptions about the formation of different NiOOH structures α/γ or β/β. These assumptions have to be confirmed by carrying out more studies with spectroscopic techniques such as in situ Raman spectroscopy or infrared spectroscopy. The macro used to automate the electrode pretreatment and

collection of sampled current voltammograms can be improved by changing some parameters such as the holding time, the initial potential, and sweeping between upper and lower cleaning potentials make sure the same surface conditions for all the experiments. It is suggested to study the self-terminated nickel electrodeposition on gold microelectrodes with the same conditions as was studied with macroelectrodes because it can offer a better point of comparison.

Bibliography

[1] Daniela van Schagen Mendoza. Opportunities in the Mexican Renewable Energy Sector. Technical report, 2018.

[2] Edgar Santoyo-Castelazo, Laurence Stamford, and Adisa Azapagic. Environmental implications of decarbonising electricity supply in large economies: The case of Mexico. *Energy Conversion and Management*, 85:272–291, 2014.

[3] Javid Mohtasham. Review Article-Renewable Energies. *Energy Procedia*, 74:1289–1297, 2015.

[4] Gibrán S. Alemán-Nava, Victor H. Casiano-Flores, Diana L. Cárdenas-Chávez, Rocío Díaz-Chavez, Nicolae Scarlat, Jürgen Mahlknecht, Jean Francois Dallemand, and Roberto Parra. Renewable energy research progress in Mexico: A review. *Renewable and Sustainable Energy Reviews*, 32:140–153, 2014.

[5] J. Nowotny, C. C. Sorrell, L. R. Sheppard, and T. Bak. Solar-hydrogen: Environmentally safe fuel for the future. *International Journal of Hydrogen Energy*, 30(5):521–544, 2005.

[6] Omar Z. Sharaf and Mehmet F. Orhan. An overview of fuel cell technology: Fundamentals and applications. *Renewable and Sustainable Energy Reviews*, 32:810–853, 2014.

[7] Cynthia G. Zoski. *Handbook of Electrochemistry*. Elsevier, Oxford, United Kingdom, 2007.

[8] B. C. Steele and Angelika Heinzel. Materials for fuel-cell technologies. *Nature*, 414(November):345–352, 2001.

[9] Sossina M. Haile. Fuel cell materials and components. *Acta Materialia*, 51(19):5981–6000, 2003.

[10] L. Carrette, K. A. Friedrich, and U. Stimming. Fuel Cells - Fundamentals and Applications. *Fuel Cells*, 1(1):5–39, 2001.

[11] S. Sarangapani, F. L. Luczak, M. Enayetullah, T. Vitella, and P. Osenar. Alkaline Direct Methanol Fuel Cell. *ECS Transactions*, 1(32):11–22, 2006.

[12] B. Cook. Introduction to fuel cells and hydrogen technology. *Engineering Science and Education Journal*, 11(6):205, 2002.

[13] Ahmed Kadhim Hussein. Applications of nanotechnology in renewable energies - A comprehensive overview and understanding. *Renewable and Sustainable Energy Reviews*, 42:460–476, 2015.

[14] Wolf Vielstich, Arnold Lamm, and Hubert A. Gasteiger. *Handbook of Fuel Cells: Fundamentals, Technology, Applications.* Wiley, New Jersey,USA, 2003.

[15] G. J. K. Acres and G. A. Hards. Electrocatalysts for fuel cells. *Philosophical Transactions of the Royal Society A: Mathematical, Physical and Engineering Sciences*, 354(1712):1671–1680, 1996.

[16] Erich Gülzow. Alkaline fuel cells: A critical view. *Journal of Power Sources*, 61(1-2):99–104, 1996.

[17] Jung Ho Wee. Applications of proton exchange membrane fuel cell systems. *Renewable and Sustainable Energy Reviews*, 11(8):1720–1738, 2007.

[18] Chunzhi He, Sanket Desai, Garth Brown, and Srinivas Bollepalli. PEM Fuel Cell Catalysts: Cost, Performance, and Durability. *The Electrochemical Society Interface*, pages 41–44, 2005.

[19] Nigel Sammes, Roberto Bove, and Knut Stahl. Phosphoric acid fuel cells: Fundamentals and applications. *Current Opinion in Solid State and Materials Science*, 8(5):372–378, 2004.

[20] Peter Heidebrecht and Kai Sundmacher. Molten carbonate fuel cell (MCFC) with internal reforming: model-based analysis of cell dynamics. *Chemical Engineering Science*, 58(3-6):1029–1036, 2003.

[21] Andrew L. Dicks. Molten carbonate fuel cells. *Current Opinion in Solid State and Materials Science*, 8(5):379–383, 2004.

[22] Nguyen Q. Minh. Solid oxide fuel cell technology - Features and applications. *Solid State Ionics*, 174(1-4):271–277, 2004.

[23] Osamu Yamamoto. Solid oxide fuel cells: Fundamental aspects and prospects. *Electrochimica Acta*, 45(15-16):2423–2435, 2000.

[24] Chao-Yang Wang. Principles of Direct Methanol Fuel Cells for Portable and Micro Power. In S Kakaç, A Pramuanjaroenkij, and L Vasiliev, editors, *Mini-Micro Fuel Cells*, pages 235–242. Springer, Dordrecht, Dordrecht, 2008.

[25] S. K. Kamarudin, F. Achmad, and W. R. W. Daud. Overview on the application of direct methanol fuel cell (DMFC) for portable electronic devices. *International Journal of Hydrogen Energy*, 34(16):6902–6916, 2009.

[26] E. Antolini and E. R. Gonzalez. Alkaline direct alcohol fuel cells. *Journal of Power Sources*, 195(11):3431–3450, 2010.

[27] Jahan Bakhsh Raoof, Reza Ojani, and Sayed Reza Hosseini. An Electrochemical Investigation of Methanol Oxidation on Nickel Hydroxide Nanoparticles. *South African Journal of Chemistry*, 6(3):47–53, 2013.

[28] Kenneth Ikechukwu Ozoemena. Nanostructured platinum-free electrocatalysts in alkaline direct alcohol fuel cells: catalyst design, principles and applications. *RSC Adv.*, 6(92):89523–89550, 2016.

[29] Tanyuan Wang, Dongliang Gao, Junqiao Zhuo, Zhiwei Zhu, Pagona Papakon-stantinou, Yan Li, and Meixian Li. Size-dependent enhancement of electrocat-alytic oxygen-reduction and hydrogen-evolution performance of MoS_2 particles. *Chemistry - A European Journal*, 19(36):11939–11948, 2013.

[30] D. Wu, W. Zhang, and D. Cheng. Facile Synthesis of Cu/NiCu Electrocata-lysts Integrating Alloy, Core–Shell, and One-Dimensional Structures for Efficient Methanol Oxidation Reaction. *American Chemical Society*, 9:19843–19851, 2017.

[31] Karim Kakaei, Mehdi D. Esrafili, and Ali Ehsani. Introduction to Catalysis. *Interface Science and Technology*, 27:1–21, 2019.

[32] Katharina Krischer and Elena R. Savinova. *Fundamentals of Electrocatalysis*, chapter 8.1.1, pages 1873–1905. American Cancer Society, 2008.

[33] Hoyoung Kim and H. K. Kim. High-Activity Electrodeposited NiW Catalysts for Hydrogen Evolution in Alkaline Water Electrolysis. *Applied Surface Science*, 349(August 2017):629–635, 2015.

[34] Fritz Scholz. *Electroanalytical Methods*. Springer, Greifswald,Germany, 2009.

[35] Allen J. Bard. *Electrochemical Methods: Fundamentals and Application*. Wiley, Hoboken, New Jersey, 2001.

[36] D. Pletcher, R. Grefff, and R. Peat. *Instrumental Methods in Electrochemistry*. Woodhead Publishing, 1997.

[37] Douglas A. Skoog. *Principios de Análisis Instrumental*. Mc Graw Hill, Madrid,España, 2001.

[38] Andrew J. Medford, Aleksandra Vojvodic, Jens S. Hummelshøj, Johannes Voss, Frank Abild-Pedersen, Felix Studt, Thomas Bligaard, Anders Nilsson, and Jens K. Nørskov. From the Sabatier principle to a predictive theory of transition-metal heterogeneous catalysis. *Journal of Catalysis*, 328:36–42, 2015.

[39] Ali Eftekhari. Tuning the electrocatalysts for oxygen evolution reaction. *Materials Today Energy*, 5:37–57, 2017.

[40] Paola Quaino, Fernanda Juarez, Elizabeth Santos, and Wolfgang Schmickler. Volcano plots in hydrogen electrocatalysis-uses and abuses. *Beilstein Journal of Nanotechnology*, 5(1):846–854, 2014.

[41] Dennis W. Bennett. Catalysis and Electrocatalysis at Nanoparticle Surfaces By Andrzej Wieckowski (University of Illinois, Urbana-Champaign), Elena R. Savinova (Boreskov Institute of Catalysis, Russian Academy of Sciences), and Constantinos G. Vayenas (University of Patras). Marcel Dekker, Inc.: New York, Basel. 2003. xviii + 970 pp. $225.00. ISBN 0-8247-0879-2. *Journal of the American Chemical Society*, 126(14):4741–4742, 2004.

[42] B. Hvolbæk, T. V. W. Janssens, B. S. Clausen, H. Falsig, C. H. Christensen, and J. K. Nørskov. Catalytic activity of Au nanoparticles. *Nano Today*, 2(4):14–18, 2007.

[43] Ding Hao, Shi Xue-Zhao, Shen Cheng-Min, Hui Chao, Xu Zhi-Chuan, Li Chen, Tian Yuan, Wang Deng-Ke, and Gao Hong-Jun. Synthesis of monodisperse palladium nanocubes and their catalytic activity for methanol electrooxidation. *Chinese Physics B*, 19(10):106104, 2010.

[44] Weicheng Liao and Shuehlin Yau. Au(111)-Supported Pt Monolayer as the Most Active Electrocatalyst toward Hydrogen Oxidation and Evolution Reactions in Sulfuric Acid. *Journal of Physical Chemistry C*, 121(35):19218–19225, 2017.

[45] Liang Liang Feng, Guangtao Yu, Yuanyuan Wu, Guo Dong Li, Hui Li, Yuanhui Sun, Tewodros Asefa, Wei Chen, and Xiaoxin Zou. High-Index Faceted Ni3S2 Nanosheet Arrays as Highly Active and Ultrastable Electrocatalysts for Water Splitting. *Journal of the American Chemical Society*, 137(44):14023–14026, 2015.

[46] Vladimir A. Isaev and Olga V. Grishenkova. Galvanostatic nucleation and growth under diffusion control. *Journal of Solid State Electrochemistry*, 17(6):1505–1508, 2013.

[47] Lian Guo and Peter C. Searson. On the influence of the nucleation overpotential on island growth in electrodeposition. *Electrochimica Acta*, 55(13):4086 – 4091, 2010.

[48] E. Budevski, G. Staikov, and W. J. Lorenz. Electrocrystallization Nucleation and growth phenomena. *Electrochimica Acta*, 45(15-16):2559–2574, 2000.

[49] Gerardo T. Martínez, Genaro Zavala, and Marcelo Videa. Electrodeposition of Nickel Particles and their Characterization. *Journal of the Mexican Chemical Society*, 53:7 – 11, 03 2009.

[50] Vladimir A. Isaev and Olga V. Grishenkova. Galvanostatic phase formation. *Journal of Solid State Electrochemistry*, 18(9):2383–2386, 2014.

[51] M. Paula Salinas-Quezada, D. Alfonso Crespo-Yapur, A. Cano-Marquez, and M. Videa. Electrocatalytic Activity of Galvanostatically DepositedNi Thin Films forMethanol Electrooxidation. *Fuel Cell*, 19(5):587–593, 2019.

[52] Rongyue Wang, Ugo Bertocci, Haiyan Tan, Leonid A. Bendersky, and Thomas P. Moffat. Self-Terminated Electrodeposition of Ni, Co, and Fe Ultrathin Films. *ACS Physical Chemistry*, 120, 2016.

[53] Yihua Liu, Dincer Gokcen, Ugo Bertocci, and Thomas P. Moffat. Self-terminating growth of platinum films by electrochemical deposition. *Science*, 338(6112):1327–1330, 2012.

[54] Nicole L. Ritzert and Thomas P. Moffat. Ultramicroelectrode Studies of Self-Terminated Nickel Electrodeposition and Nickel Hydroxide Formation upon Water Reduction. *ACS Physical Chemistry*, 120:27478–27489, 2016.

[55] Wenjing Huang, Hongtao Wang, Jigang Zhou, Jian Wang, Paul N. Duchesne, David Muir, Peng Zhang, Na Han, Feipeng Zhao, Min Zeng, Jun Zhong, Chuanhong Jin, Yanguang Li, Shuit Tong Lee, and Hongjie Dai. Highly active and durable methanol oxidation electrocatalyst based on the synergy of platinum-nickel hydroxide-graphene. *Nature Communications*, 6:1–8, 2015.

[56] Dayi Chen and Shelley D Minteer. Mechanistic study of nickel based catalysts for oxygen evolution and methanol oxidation in alkaline medium. *Journal of Power Sources*, 284:27–37, 2015.

[57] Bruno G. Pollet. *Polymer Electrolyte Membrane and Direct Methanol Fuel Cell Technology*, volume 57. Johnson Matthey PLC, 2013.

[58] G. A. Tritsaris and J. Rossmeisl. Methanol oxidation on model elemental and bimetallic transition metal surfaces. *Journal of Physical Chemistry C*, 116(22):11980–11986, 2012.

[59] T. Iwasita. Electrocatalysis of methanol oxidation. *Electrochimica Acta*, 47:3663–3674, 2002.

[60] Claudio Bianchini and Pei Kang Shen. Palladium-based electrocatalysts for alcohol oxidation in half cells and in direct alcohol fuel cells. *Chemical Reviews*, 109(9):4183–4206, 2009.

[61] Qian Jiang, Luhua Jiang, Jing Qi, Suli Wang, and Gongquan Sun. Experimental and density functional theory studies on PtPb/C bimetallic electrocatalysts for methanol electrooxidation reaction in alkaline media. *Electrochimica Acta*, 56(18):6431–6440, 2011.

[62] Ludo Juurlink. Stepped surfaces. *Journal of Physics Condensed Matter*, 30(9), 2018.

[63] Eileen Hao Yu, Keith Scott, and Robert W. Reeve. A study of the anodic oxidation of methanol on Pt in alkaline solutions. *Journal of Electroanalytical Chemistry*, 547(1):17–24, 2003.

[64] Honghui Guo, Zhengjun Huang, Yanjie Zheng, and Shaohuang Weng. Electrodeposition of Nickel Nanoparticles Modified Glassy Carbon Electrode for Nonenzymatic Glucose Biosensing. *International Journal of Electrochemical Science*, 10:10703–10712, 2015.

[65] M. A. Abdel Rahim, R. M. Abdel Hameed, and M. W. Khalil. Nickel as a catalyst for the electro-oxidation of methanol in alkaline medium. *Journal of Power Sources*, 134(2):160–169, 2004.

[66] Ahmad Nozad Golikand, Saeed Shahrokhian, Mehdi Asgari, Mohammad [Ghannadi Maragheh], Leila Irannejad, and Alireza Khanchi. Electrocatalytic oxidation of methanol on a nickel electrode modified by nickel dimethylglyoxime complex in alkaline medium. *Journal of Power Sources*, 144(1):21 – 27, 2005.

[67] Neeta L. Lala, Velmurugan Thavasi, and Seeram Ramakrishna. Preparation of surface adsorbed and impregnated multi-walled carbon nanotube/nylon-6 nanofiber composites and investigation of their gas sensing ability. *Sensors*, 9(1):86–101, 2009.

[68] M. Lukaszewski, M. Soszko, and A. Czerwiński. Electrochemical methods of real surface area determination of noble metal electrodes - an overview. *International Journal of Electrochemical Science*, 11(6):4442–4469, 2016.

[69] Samuel C. Perry, Laila Al. Shandoudi, and Guy Denuault. Sampled-Current Voltammetry at Microdisk Electrodes: Kinetic Information from Pseudo Steady State Voltammograms. *Analytical Chemistry*, 86:9917–9923, 2014.

[70] Laila AL-Shandoudi. Transient Studies of Oxygen Reduction At Microelectrodes. *Engineering Sciences*, page 194, 2015.

[71] Strecková M. Orináková, R. and Gálová M. Comparison of chloride and sulphate electrolytes in nickel electrodeposition on a paraffin impregnated graphite electrode. *Journal of Electroanalytical Chemistry*, 594:152–159, 2006.

[72] M. R. Barbosa, J. A. Bastos, J. J. Â Garc, and F Vicente. Chloride role in the surface of nickel electrode. *Electrochemica Acta*, 44:957–965, 1998.

[73] Petr Vanýsek. Ionic conductivity and diffusion at infinite dilution. *CRC Handbook of Chemistry and Physics*, 96(73):5–98, 1996.

[74] Yundan Yu, Lixia Sun, Hongliang Ge, Guoying Wei, and Li Jiang. Study on electrochemistry and nucleation process of nickel electrodeposition. *International Journal of Electrochemical Science*, 12(1):485–495, 2017.

[75] Allen Bai and Chi Chang Hu. Effects of electroplating variables on the composition and morphology of nickel-cobalt deposits plated through means of cyclic voltammetry. *Electrochimica Acta*, 47(21):3447–3456, 2002.

[76] Niladri Roy Chowdhury, Ratnesh Kumar, and Rama Kant. Theory for the chronopotentiometry on rough and finite fractal electrode: Generalized Sand equation. *Journal of Electroanalytical Chemistry*, 802:64–77, 2017.

[77] W. H. Reinmuth. Distortion of Chronopotentiograms from Double Layer and Surface Roughness Effects. *Analytical Chemistry*, 33(4):485–487, 1961.

[78] Yu Zhi Su, Kang Xiao, Nan Li, Zhao Qing Liu, and Shi Zhang Qiao. Amorphous $Ni(OH)_2$ @ three-dimensional Ni core-shell nanostructures for high capacitance pseudocapacitors and asymmetric supercapacitors. *Journal of Materials Chemistry A*, 2(34):13845–13853, 2014.

[79] H. Bode, K. Dehmelt, and J. Witte. Zur kenntnis der nickelhydroxidelektrode-I. Über das nickel (II)-hydroxidhydrat. *Electrochimica Acta*, 11(8):1079–1087, 1966.

[80] Fabio Dionigi and Peter Strasser. NiFe-Based (Oxy)hydroxide Catalysts for Oxygen Evolution Reaction in Non-Acidic Electrolytes. *Advanced Energy Materials*, 6(23):1–20, 2016.

[81] Špela Trafela, Janez Zavašnik, Sašo Šturm, and Kristina Žužek Rožman. Formation of a Ni(OH)2/NiOOH active redox couple on nickel nanowires for formaldehyde detection in alkaline media. *Electrochimica Acta*, 309:346–353, 2019.

[82] P. Oliva, J. Leonardi, J. F. Laurent, C. Delmas, J. J. Braconnier, M. Figlarz, F. Fievet, and A. de Guibert. Review of the structure and the electrochemistry of nickel hydroxides and oxy-hydroxides. *Journal of Power Sources*, 8(2):229–255, 1982.

[83] Yoshio Takasu, Yuichi Fujii, Koso Yasuda, Yukinori Iwanaga, and Yoshiharu Matsuda. Electrocatalytic properties of ultrafine platinum particles for hydrogen electrode reaction in an aqueous solution of sulfuric acid. *Electrochimica Acta*, 34(3):453–458, 1989.

[84] M. Fleischmann, K. Korinek, and D. Pletcher. The oxidation of organic compounds at a nickel anode in alkaline solution. *Journal of Electroanalytical Chemistry*, 1971.

[85] Boon Siang Yeo and Alexis T Bell. In Situ Raman Study of Nickel Oxide and Gold-Supported Nickel Oxide Catalysts for the Electrochemical Evolution of Oxygen. *Physical Chemistry C*, 116:8394–8400, 2012.

[86] Yu Jen Shih, Yao Hui Huang, and C. P. Huang. In-situ electrochemical formation of nickel oxyhydroxide (NiOOH) on metallic nickel foam electrode for the direct oxidation of ammonia in aqueous solution. *Electrochimica Acta*, 281:410–419, 2018.

[87] Robert Kostecki. Electrochemical and In Situ Raman Spectroscopic Characterization of Nickel Hydroxide Electrodes. *Journal of The Electrochemical Society*, 144(2):485, 1997.

[88] S. M. Golabi and A. Nozad. Electrocatalytic oxidation of methanol on a nickel-porphyrin IX complex modified glassy carbon electrode in alkaline medium. *Electroanalysis*, 16(3):199–209, 2004.

[89] J. Taraszewska and G. Roslonek. Electrocatalytic oxidation of methanol on a glassy carbon electrode modified by nickel hydroxide formed by ex situ chemical precipitation. *Journal of Electroanalytical Chemistry*, 364:209–213, 1994.

[90] Meisong Guo, Yanan Yu, and Jingbo Hu. Nickel Nanoparticles for the Efficient Electrocatalytic Oxidation of Methanol in an Alkaline Medium. *Electrocatalysis*, 8(4):392–398, 2017.

[91] Yuqing Miao, Lei Ouyang, Shilin Zhou, Lina Xu, Zhuoyuan Yang, Mingshu Xiao, and Ruizhuo Ouyang. Electrocatalysis and electroanalysis of nickel, its oxides, hydroxides and oxyhydroxides toward small molecules. *Biosensors and Bioelectronics*, 53:428–439, 2014.

[92] I. Danaee, M. Jafarian, F. Forouzandeh, F. Gobal, and M. G. Mahjani. Electrochemical impedance studies of methanol oxidation on GC/Ni and GC/NiCu electrode. *International Journal of Hydrogen Energy*, 34(2):859–869, 2009.

[93] Neil Spinner and William E. Mustain. Effect of nickel oxide synthesis conditions on its physical properties and electrocatalytic oxidation of methanol. *Electrochimica Acta*, 56(16):5656–5666, 2011.

[94] B. Shruthi, B. J. Madhu, V. Bheema Raju, S. Vynatheya, B. Veena Devi, G. V. Jayashree, and C. R. Ravikumar. Synthesis, spectroscopic analysis and electrochemical performance of modified β-nickel hydroxide electrode with CuO. *Journal of Science: Advanced Materials and Devices*, 2(1):93–98, 2017.

[95] David S. Hall, David J. Lockwood, Christina Bock, and Barry R. MacDougall. Nickel hydroxides and related materials: A review of their structures, synthesis and properties. *Proceedings of the Royal Society A: Mathematical, Physical and Engineering Sciences*, 471(2174), 2015.

[96] A. Delahaye-Vidal, B. Beaudoin, N. Sac-Epée, K. Tekaia-Elhsissen, A. Audemer, and M. Figlarz. Structural and textural investigations of the nickel hydroxide electrode. *Solid State Ionics*, 84(3-4):239–248, 1996.

[97] Michael E.G. Lyons and Michael P. Brandon. The oxygen evolution reaction on passive oxide covered transition metal electrodes in aqueous alkaline solution. Part 1-Nickel. *International Journal of Electrochemical Science*, 3(12):1386–1424, 2008.

[98] Tao Yang, Lijuan Zhang, Xiang Li, and Dingguo Xia. Structural and morphological characterization of gold-nickel electrocatalyst synthesized by taking advantage of the AuNi phase separation mechanism. *Journal of Alloys and Compounds*, 492(1-2):83–87, 2010.